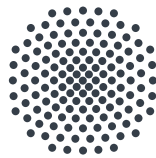Bachelor Thesis

An optical setup for the direct laser cooling of molecules

Benjamin Renz

Version 1.1
24.10.2020

Examiner: Prof. Dr. Tilman Pfau
co-supervisor: Dr. Tim Langen

University of Stuttgart
5th Institute of Physics

Deutsche Zusammenfassung

Ziel dieser Bachelorarbeit ist der Aufbau eines Lasersystems, um die Anzahl an gestreuten Photonen an einem Bariumfluorid-Molekülstrahl gegenüber einem existierenten Aufbau zu erhöhen. Bariummonofluorid benötigt zur Kühlung einen Hautkühllaser und mehrere Repumplaser um den Verlust von Molekülen in dunkle, nicht durch Laser addressierte Zustände zu minimieren. Moleküle besitzen im Vergleich zu Atomen keine geschlossene Kühlübergänge, durch den Zerfall in höhere Vibrationszustände ist die Anzahl an Photonenstreuungen begrenzt. Der Hauptkühllaser kann die Molelküle in den zusätzlichen Vibrationszuständen nicht mehr anregen und somit sind diese nicht mehr zur Kühlung nutzbar. Mit dem neu gebauten Repumplaser mit der Wellenlänge $\lambda = 900.243\,\text{nm}$ können Moleküle aus dem $\nu = 3$ Vibrationszustand wieder dem Kühlschema zugeführt werden. Durch die Erhöhung der Anzahl der gestreuten Photonen auf mehr als 1000 sind ausreichend niedrige Geschwindigkeitsbereiche zugänglich, um die Moleküle beispielsweise mit magnetooptischen Fallen für neue Experimente nutzbar zu machen.

Mittels eines Gratings und einer GaAs-Laserdiode wurde dieses frequenzabstimmbare Lasersystem aufgebaut. Es wurde hinsichtlich Linienbreite, P-I-Kurve, Strahlprofil und Sprungverhalten bei Temperatur und Stromänderung charakterisiert.Die Exzentrizität im Strahlprofil wurde durch ein Prismenpaar korrigiert. Der ohne Modensprung einstellbare Frequenzbereich wurde anhand der Positionierung des Gratings und dem daraus ableitbaren Rotationspunkt bestimmt. Mit dem Ziel den Laser für länger andauernde Experimente in seiner Frequenz zu stabilisieren, wurden zwei Fabry-Pérot Resonatoren charakterisiert. Einer dieser Resonatoren wurde nach einem am 5. Physikalischen Institut entworfenen Design aufgebaut, der andere war bereits Teil des bestehenden Versuchsaufbaus. Das Rauschverhalten des Scansignals beider Resonatoren wurde verglichen. Der Resonator mit besserem Rauschverhalten wurde dann für eine Langzeitstabilisation des Lasers mittels des Pound-Drever-Hall Verfahrens verwendet. Dafür kamen die FPGA-Entwicklungsplatine "Stemlabs 125-14" und das quelloffene Programm "linien" zum Einsatz. Diese Entwicklungsplatform wurde zudem genutzt um die Nichtlinearität des Piezos dieses Resonators zu vermessen.

Abstract

The goal of this thesis is the construction of a diode laser system. It is used to increase the achievable number of scattered photons on a molecular beam in an existing laser cooling experiment. The molecule of choice, barium monofluoride, requires one main cooling laser and multiple repump lasers to avoid losing molecules to dark, unaddressed states. In contrast to atoms, molecules feature many vibrational states, to which some molecules are lost. Repump lasers can bring the population in these states back into the cooling cycle. The laser presented in this thesis is the third repump laser with a wavelength of $\lambda = 900.243\,\mathrm{nm}$. It closes leaks to the $\nu = 3$ vibrational state, which should facilitate the scattering of more than 1000 photons per molecule, and, hence, make the molecules slow enough for magneto-optical trapping. By cooling molecules to such low temperatures, they can be used for new experiments.

This frequency tunable lasersystem is created by combining a GaAs-diode laser with a rotatable Blaze-grating. It is characterized in terms of linewidth, optical output power, beamprofile, and modehop behavior for varying temperature and current. The excentricity of the resulting beam required the correction with an anamorphic prism pair.

To use the laser for experiments with longer duration, the laser needs to be stabilized in terms of frequency. This was achieved by stabilizing it to a Fabry-Perot resonator using the Pound-Drever-Hall scheme. This stabilization was realized using the FPGA development board "Stemlabs 125-14" in conjunction with the open source locking software "linien". This development platform was further used to characterize the non-linear response of the piezoelectric actuator in the cavity and study noise sources that could limit the final frequency stability of the laser.

Contents

1 Motivation

Since the first cooling of Ba⁺ ions [1] in 1978 the use of laser cooling has expanded to neutral atoms [2] and diatomic molecules [3]. With the advancement in cooling technology atomic clocks can be constructed with record breaking accuracy [4], individual atoms can be manipulated using optical tweezers [5], and atomic gases can be cooled to quantum degeneracy [6].

However, due to their complex level structure, experiments on molecules have been limited to proof of concept experiments so far. Further improvements in cooling methods for even the simplest molecules formed from two atoms can therefore vastly expand the range of possible experiments. In comparison to atoms, diatomic molecules can feature large permanent electric dipole moments. Therefore ultracold molecules would have extremely large dipole-dipole-interactions making them interesting for use in quantum simulation [7] [8].
Moreover, molecules form the basic building blocks of chemical reactions. Cooling them to these temperatures enables the precise control over the molecular dipole moments of ultracold molecules which opens the possibility to study chemical reactions with full quantum state control [9]. Ultracold molecules can further be used to conduct precision measurements on the variation of fundamental constants [10] [11], for the search of the electron's hypothetical permanent electric dipole moment [12] or for checking the spin-dependent parity violation effect [13].

A particularly interesting molecule for such precision measurements is barium monofluoride (BaF) [14]. Barium monofluoride's energy level structure permits relatively simple laser cooling schemes, as losses in unwanted Δ states are predicted to be at an almost negligible level [15].

In the following a laser system is presented which will help to prepare an experiment at the 5th Physics Institute for the realization of the first laser cooling of barium monofluoride molecules.

2 Background

2.1 Laser cooling of molecular beams

Laser cooling describes a process where atoms or molecules are cooled by absorbing and re-emitting photons. When directional light sources are used, the absorption of a photon always transfers momentum in the direction of the light source. The direction of spontaneous emission is randomly distributed in all spatial directions, hence on average, the particle experiences a force F_{scatter} in the direction of the incoming light. Absorption and emission of the photons is mainly determined by the energy level structure of the atom or molecule.

In the simplest setting, this can be used to slow down a beam of particles or deflect molecular beams. By repeating this process many more times a reduction in forward velocity of the particles in the molecular beam occurs. A more complex situation arises when the force acting on the particles should not only be applied in one direction, but rather in the opposite direction of movement. This enables a possibility to cool a stationary cloud of molecules which, in a simple 1-dimensional picture, has particles moving in different directions. In low pressure regimes the velocities of molecular ensembles are distributed according to a Maxwell-Boltzmann velocity distribution [17], which means that the average velocity $\bar{v}$, on top of the movement velocity of the molecular beam, is given by [17]

$$\bar{v} = \sqrt{\frac{8 \cdot k_b \cdot T}{\pi \cdot m}}. \tag{1}$$

The equation sets this average velocity in relation with the temperature T, the Boltzmann constant k_b and the mass m of the particles. To cool particles in one dimension, independent of their movement direction, one can employ Doppler cooling. This cooling technique uses the shift in frequency that a particle sees in their moving frame of reference due to the relativistic Doppler effect.

Two counterpropagating lasers are overlapped, emitting photons in opposite directions. They are both red-detuned to cooling transition's frequency (refer to figure 2). When a particle moves opposite to the direction of one beam its light will get blue-detuned. The transition will therefore be excited much stronger by this laser than from the red-detuned light from the other laser. Therefore the particle's momentum is reduced. Overall, the velocities of all particles in the distribution are thus reduced and the ensemble is cooled.
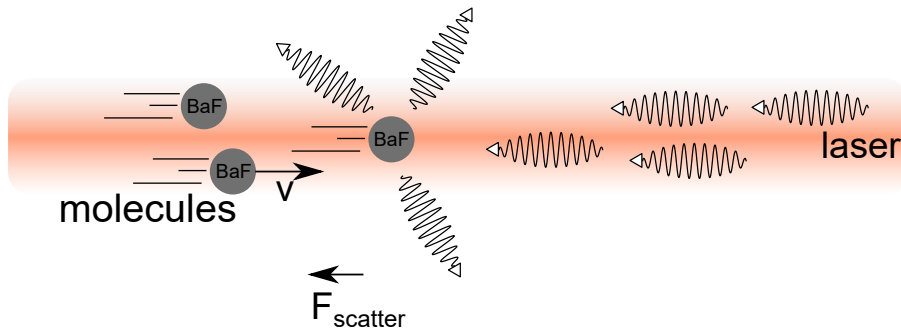

Figure 1: Schematic process of scattering photons on barium monofluoride molecules to achieve slowing of the molecules. Photons of the laser and scattered photons are illustrated by the oscillating lines. The figure was adapted from [16].
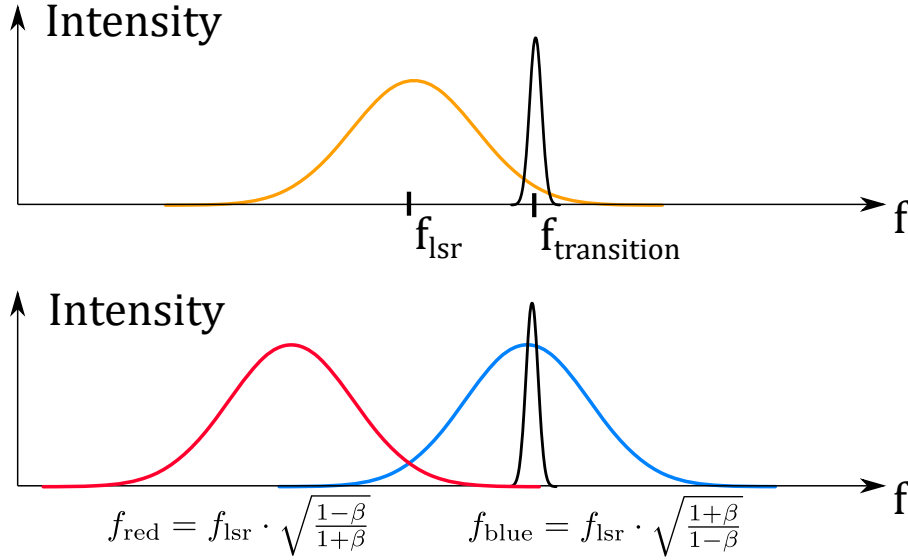
Figure 2: Illustation of Doppler cooling and the corresponding frequency shifts. The upper illustration shows the case of a particle at rest in comparison to the transition frequency $f_{\text{transition}}$ and red-detuned laser frequency f_{lsr}. In the lower picture, the particle is moving with the velocity of $v = \beta \cdot c$. The frequency of one laser is blue-shifted and therefore closer to the transition frequency while the red-shifted laser's frequency f_{red} has moved further away from $f_{\text{transition}}$.

2.2 Transitions and level structure of BaF

To achieve closed-cycle cooling transitions, a two level system is preferable, which can then be excited by a cooling laser. In comparison to atoms, molecules have a more complicated level structure because they have additional vibrational and rotational degrees of freedom. This means, that many more levels have to be taken into account to describe the interaction of molecules and light. The following section will introduce the important features of these spectra and how laser-cooling can still be possible.

To calculate these spectra the Born-Oppenheimer approximation can be used, which separates the electron movement from the movement and vibration of the nuclei [18]. By using a product ansatz for the wave function $\Psi = \Psi_{\text{elec}}(\mathbf{r}_i) \cdot \Psi_{\text{vibr}}(\mathbf{R}_i)$, where the electronic part of the wave function only depends on the position operators of the electrons, and the vibrational part depends only on the positions of the nuclei. The probability amplitude of a transition between two different states is then calculated as follows:

$$P = \int \Psi'^* \mu \Psi \tag{2}$$
$$= \underbrace{\int \Psi'^*_{\text{vibr}} \Psi_{\text{vibr}}}_{\text{Franck-Condon factor}} \cdot \underbrace{\int \Psi'^*_{\text{elec}} \mu \Psi_{\text{elec}}}_{\text{orbital selection rule}}$$

where Ψ and Ψ' are the wavefunctions of the initial and the final state and μ being the molecular dipole operator.

According to [19] 10^4 photons must be scattered in order to cool BaF from a cryogenic buffer gas source. As mentioned, laser cooling is made particularly challenging for molecules, since so-called close-cycle transitions are rare for molecules due to the far greater amount of possible

3

transitions caused by vibrational and rotational branching. A closed-cycle transition is a series of absorption and spontaneous emission processes where no transition leads to an unaddressed state. In such a cycle an infinite amount of photons can be scattered by the molecule which is cooled.

To maximize the number of scattered photons and avoid loosing molecules into unaddressed states it's important to understand the transitions and energy level structure of $^{138}Ba^{19}F$.

Figure 3a depicts a simplified level scheme for BaF, including states with vibrational numbers less than 4. The main cooling transition is the one starting from the ground state $X^2\Sigma_{1/2}$ with the vibrational quantum number $\nu = 0$ into the excited state $A^2\Pi_{1/2}$ with $\nu = 0$. Due to the absence of a selection rule for these vibrational transitions, the excited state will decay into electronic ground states with different vibrational quantum numbers. For barium monofluoride the Franck Condon factors have been taken from [20].

(a)

(b)
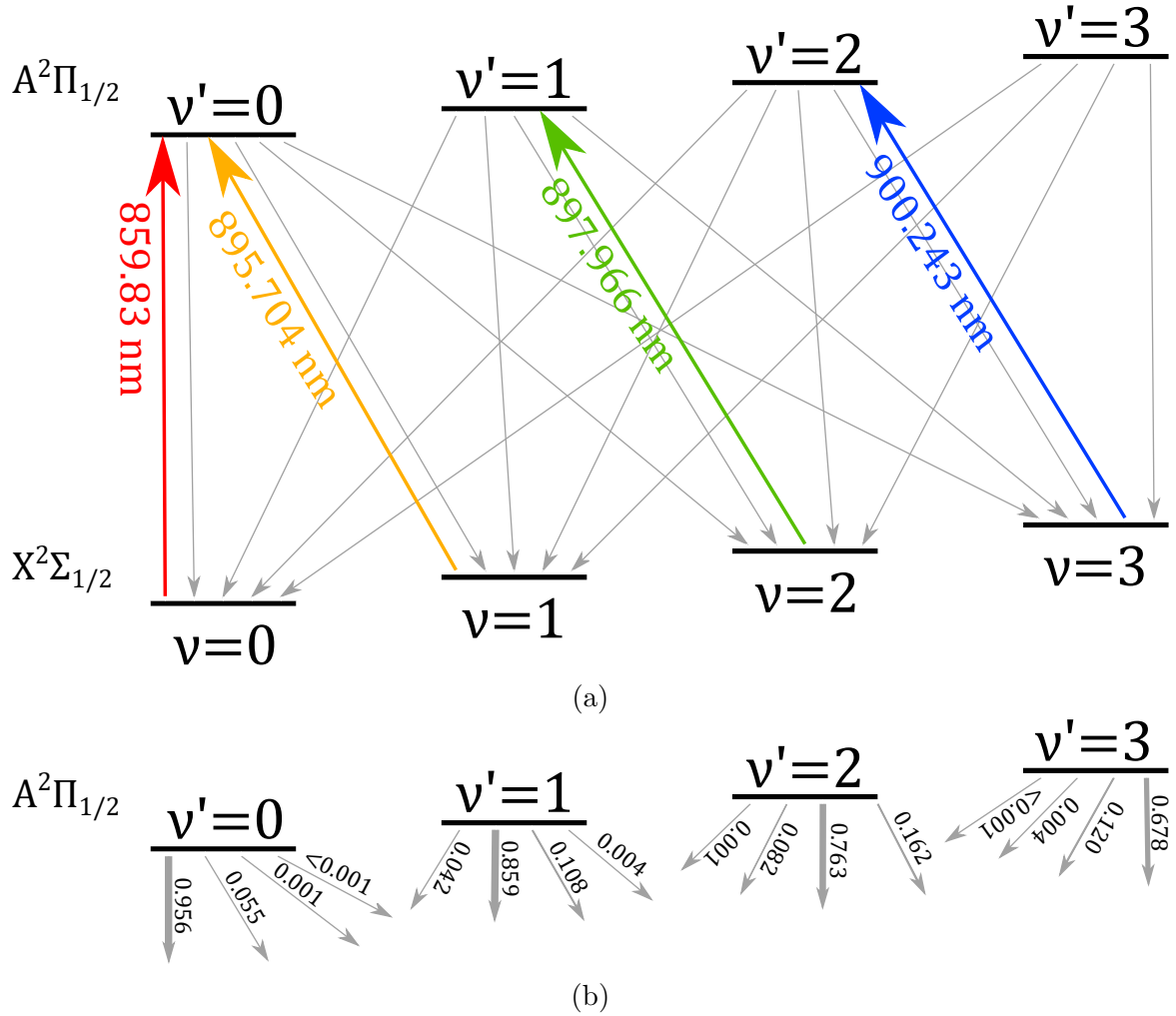
Figure 3: (a) Schematic representation of the energy levels of $^{138}Ba^{19}F$. The main cooling transition is illustrated as a red arrow, while the repump transitions are colored orange,green and blue in ascending order. The laser built in this thesis is the third repump laser (blue). Please note that these energy levels are further split by the fine- and hyperfine-structure.

(b) Franck-Condon factors (FCFs) from the transitions from the $A^2\Pi_{1/2}$ to the $X^2\Sigma_{1/2}$ states for $\nu < 4$. One can clearly see that the FCFs are highly diagonal, as indicated by the linewidth of the arrows for transitions between states with same vibrational number. The probability of decay into the ground state with the same vibrational number decreases with with increasing ν.

4

Without the repump lasers molecules from inside the cooling cycle between the ground state $\nu = 0$ and the excited state $\nu' = 0$ will decay into states that are not addressed by cooling lasers. So multiple repumping lasers are in place which transfer the molecules from the states $\nu \neq 0$ into the state $\nu' = 0$. The more states are addressed by repumping lasers the less molecules are lost into unaddressed states and the number of scattered photons summed over the whole cooling process increases as illustrated in figure 4. The current experimental setup consists of one main cooling laser (illustrated in red) and two repump lasers (illustrated in orange and green). Figure 4 indicates that the third repump laser will raise the number of scattered photons by a factor of ≈ 10. It will be built and characterized in the following chapter.
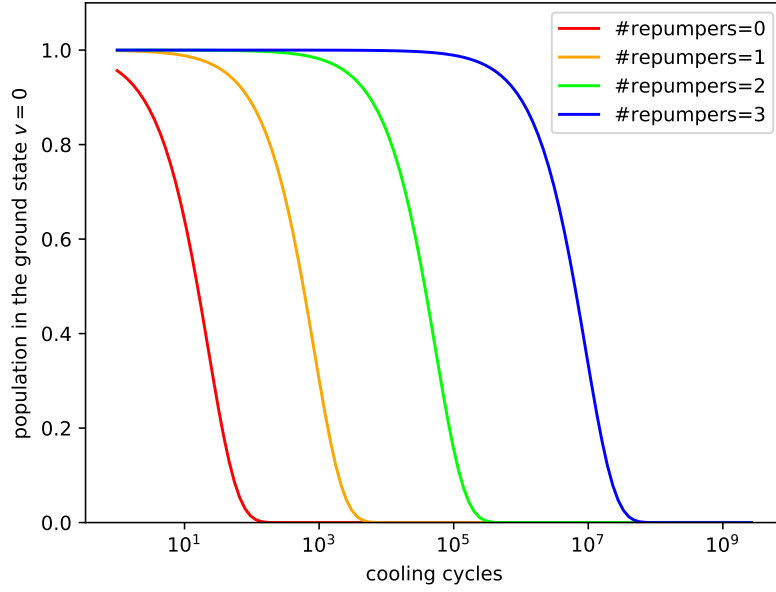

Figure 4: Population of the $X^2\Sigma_{\frac{1}{2}}(\nu = 0)$ ground states as a function of the number of scattered photons. Adding repump lasers greatly increases the number of scattered photons before losses to dark states start to drastically decrease the population. The Franck Condon factors are taken from [21]. The graphs only give a rough estimate of the required photons, since the simulation method only accounts for losses from the state $\Pi_{1/2}$ $v' = 0$.

2.2.1 Additional physical properties of barium monofluoride

In the current experimental setup barium monofluoride molecules are created by laser ablation from an pressed powder pallet consisting of BaF_2 [20]. These molecules have a mass of $156.325\,\text{u}$ [22] and are cooled with a He-Buffer gas. These molecules are radicals, which do not exist for long or under normal atmospheric conditions, since they are highly reactive [20]. When they enter the vacuum tube their mean forward velocity is only $190\,\text{m s}^{-1}$ [20]. The mass of the molecule depends on it's isotope composition. Fluorine has only one stable isotope [23] and the most abundant isotope of barium is ^{138}Ba with an percentage in terrestrial samples of 71.699% [23]. The most prevalent molecule ^{138}Ba^{19}F is a bosonic molecule, since its total spin is an integer number:

$$S_{\text{total}} = (N_{\text{electrons}} + N_{\text{protons}} + N_{\text{neutrones}}) \cdot \frac{1}{2} = ((56+9) + (56+9) + (82+10)) \cdot \frac{1}{2} = 111.$$

It has a dipole moment of 3.17 D [24], making barium monofluoride an interesting candidate in quantum simulation applications. Its high mass makes it also a highly sensitive tool for precision tests.

2.3   Working principle of an external cavity diode laser

Lasers are typically used as the light source for cooling since all their power is distributed over a small frequency band. This means that they are well suited to drive the narrow transitions of atoms and molecules while requiring drastically less energy compared to a white light source. The goal is now to construct the third repump laser, which's frequency is tunable to excite the transitions mentioned in chapter 2.2. To construct such a laser with an externally adjustable frequency, a semiconductor laser diode can be combined with an external cavity which filters out one specific laser mode and reflects it back into the diode to favor this mode. A compact way to create such an adjustable cavity is the use of a diffraction grating in the Littrow configuration. In the following chapter the correct position of such a grating for the desired wavelength is calculated. Furthermore, beam shaping correction calculations with prism pairs are presented, which are potentially needed to correct for a ellipticity of the beam's profile.

2.3.1   Resulting requirements for the third repump laser

The repump laser needs to have a wavelength of $\lambda = 900.243\,\mathrm{nm}$ in order to excite the transition described in chapter 2.2. Since the laser's power is increased with a tapered amplifier the power requirement of the laser is the sum of the required seed power for the tapered amplifier and the power extracted before the amplifier for the locking branch. The power required for seeding for a typical tapered amplifier ranges from $10\,\mathrm{mW}$ to $50\,\mathrm{mW}$ [25]. For the locking branch less than $1\,\mathrm{mW}$ optical power is required. Therefore a laser with a minimum output power of $20\,\mathrm{mW}$ is sufficient, when accounting for losses in the optical setup. The linewidth requirements posed on such a laser system is to have a similar or smaller linewidth than the transitions it is going to drive. The linewidth of those transitions can be estimated with the lifetimes of the states in [15] to be around $\Delta f_{\mathrm{transition}} = 2\,\mathrm{MHz}$.

2.3.2 Littrow configuration and grating positioning

In the Littrow configuration the grating is positioned in such a way that an incident beam from the laser diode is overlapped with the outgoing ray of the first negative diffraction order.
In order to calculate this angle, the relation between the grating linewidth d, the wavelength λ and the angle θ and the order of diffraction n must be derived.

(a) ray traces for the general diffraction orders of a blazed grating

(b) schematic for the calculation of path differences for incoming parallel rays

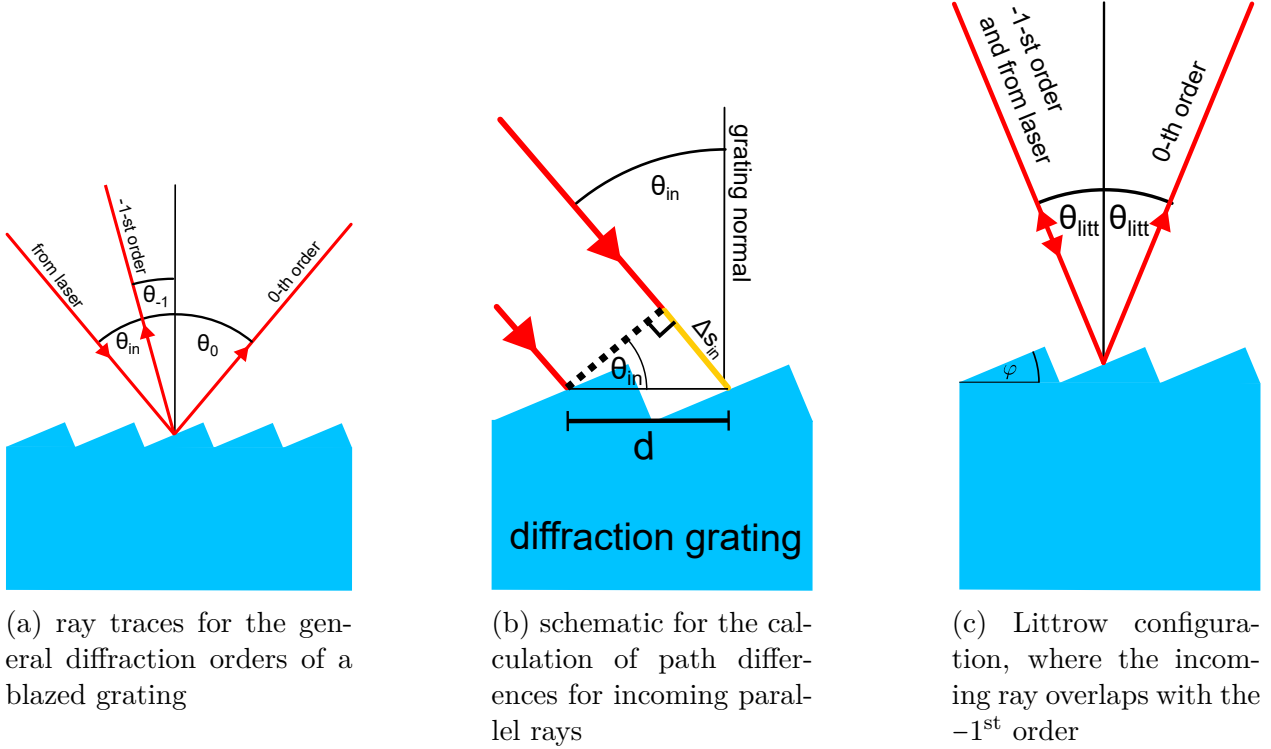(c) Littrow configuration, where the incoming ray overlaps with the -1st order

Figure 5: Illustrations of ray traces on a blazed grating for different cases

The condition for the occurrence of a diffraction order n is

$$\Delta s_{\text{total}} = n \cdot \lambda \tag{3}$$

with n being an integer. For the naming convention for diffraction orders please refer to figure 5a.
To simplify the calculation of the path difference one can first calculate the path difference of two incoming beams to the surface of the grating Δs_{in} (see figure 5b). This path difference is

$$\Delta s_{\text{in}} = \sin(\theta_{\text{in}}) \cdot d \tag{4}$$

since Δs and d occur in a right triangle in which the angle of the incoming ray to the grating normal θ_{in} is also present. The path difference from the surface for the outgoing ray can be derived analogous and is

$$\Delta s_{\text{out}} = \sin(\theta_{\text{out}}) \cdot d. \tag{5}$$

Substituting the summed path differences $\Delta s_{\text{total}} = \Delta s_{\text{in}} + \Delta s_{\text{out}}$ in equation 3 leads to [26]

$$d \cdot (\sin(\theta_{\text{in}}) + \sin(\theta_{\text{out}})) = n \cdot \lambda. \tag{6}$$

For the Littrow configuration $\theta_{\text{in}} = \theta_{\text{out}} = \theta_{\text{litt}}$, since the incoming ray overlaps the outgoing ray. Equation 6 in case of this configuration will become:

$$\theta_{\text{litt}} = \arcsin\left(\frac{\lambda}{2 \cdot d}\right) = \arcsin\left(\frac{900.243\,\text{nm}}{2 \cdot \frac{1}{1200}\,\text{mm}}\right) = 32.69° \tag{7}$$

For the desired wavelength of $\lambda = 900.243\,\text{nm}$ and the used grating with 1200 grooves/mm this results in a Littrow angle of $\theta_{\text{litt}} = 32.69°$.

During manufacturing, a step angle of a blazed grating can be optimized for a specific wavelength so that the steps' normal points into the direction of the incoming and outgoing beam. The blaze angle φ is this angle under which the maximum intensity is observable. It should be as close as possible to the Littrow angle θ_{litt}, so that most of the reflected power goes into the -1st diffraction order. The grating used is the Thorlabs GR13-1208 with a blaze angle of $\varphi = 26°44'$

2.3.3 Pivot point calculation

To avoid mode hopping when turning the grating to adjust the feedback mode, it is important that the following conditions are satisfied [27]:

- When the grating is moved, the incoming and outgoing angles still are equal but are slightly changed. Equation 7 still needs to hold for the desired detuned wavelength λ.

- Since the pivot point of the grating's rotations does not lie in the same spot where the laser hits the grating the length of the cavity created by the grating and the laser diode must change in such a way that the reflected beam path always has the length $b = \lambda \cdot c$ where c is an arbitrary but fixed constant.

If the second condition is violated, and the cavity length changes by more than $\frac{\lambda}{2}$, a mode hop will occur, limiting the possible tuning range [28]. Two distances need to be known to calculate the tuning range at a given pivot point P. When tuning the wavelength by applying a voltage to the piezo or turning the fine adjustment screw, the grating will rotate around this point P. The offset from the grating's forward face to a parallel plane through the pivot point denoted as f and the distance from the laser diode to the grating's surface L, both visualized in figure 6.
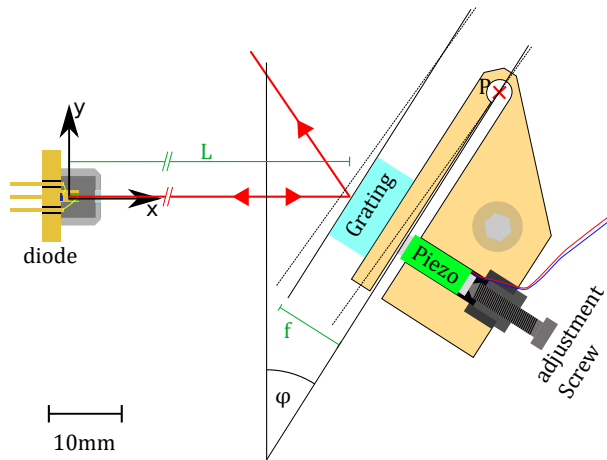

Figure 6: Construction of the grating-holder. The figure is true to scale. With the fine adjustment screw and the piezoelectric actuator, the front plate of the grating holder is rotated around the pivot point P. This changes the angle φ of the grating and the laser as well as the length of the cavity formed by the diode and the grating.

In case of the built laser $L = 27.4\,\text{mm}$ and $f = 9.7\,\text{mm}$. The pivot point of the laser is at $(58.5\,\text{mm}, 14.6\,\text{mm})$, which results in a theoretical tuning range of $4.25\,\text{pm}$ or $1.57\,\text{GHz}$.
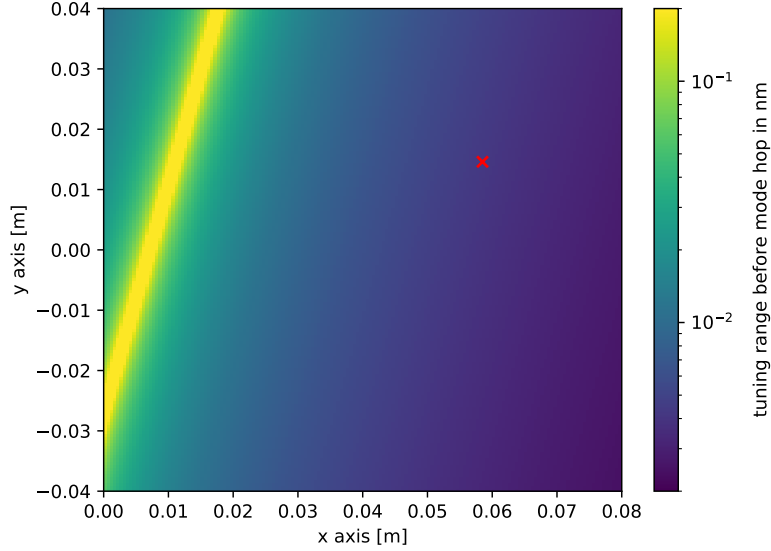

Figure 7: Plot of the tuning range in nm for different positions of the grating's pivot point. There is a line on which the laser has a high tuning range (colormap is clipping in this section). This line represents the points where the grating's parallel plane intersects with the diode chip, so putting the pivot point there is not practical. The actual position of the grating is marked with a red cross.

2.3.4 Gaussian beam-shaping by prism pairs

To maximize the coupling efficiency into an optical single mode fiber the laser beam needs to be ideally Gaussian. Deviations from a Gaussian beam shape results in reduced coupling efficiencies. Typically, the emission of a laser diode is elliptical and the reflection from the grating's surface also affects the beam's shape [29]. This ellipticity can be corrected with a pair of prisms.

The angle of refraction on the glass surface can be calculated with Snell's law with the approximation that $n_\text{air} = 1$. $n_\text{glass} = 1.760$ at $900.243\,\text{nm}$ for the N-SF11 glass that is used by the Thorlabs PS871-B anamorphic prism pair. Figure 8a shows the relation between the angle of the prism to the incoming beam and the resulting angle of the outgoing ray, with the incoming beam being parallel to the x-axis. Since the outgoing beam should be parallel to the incoming ray after the recircularization, the angles of the two prisms are restricted to values where this is the case. Because there are always two angles where the beam is deflected by the same amount, while the beam diameter changes differently for the two angles. One of the prisms is placed at the first angle α_1 and the other one at the corresponding angle α_2, depending on the desired magnification.
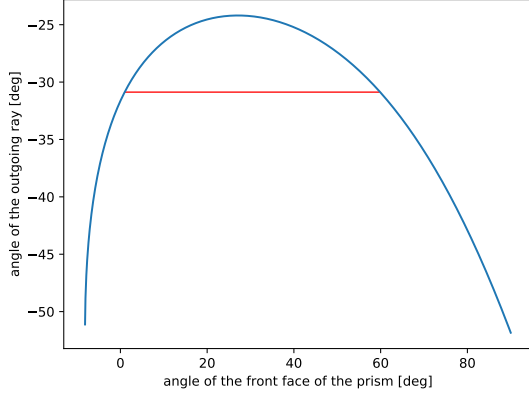
(a) Simulation of the refraction inside a prism with varying angle of incidence. There are always two angles which deflect the beam by the same total angle. The angle of the prism is measured between the surface normal facing the laser and the incoming ray. Total internal reflection occurs at the angles where the graph ends.
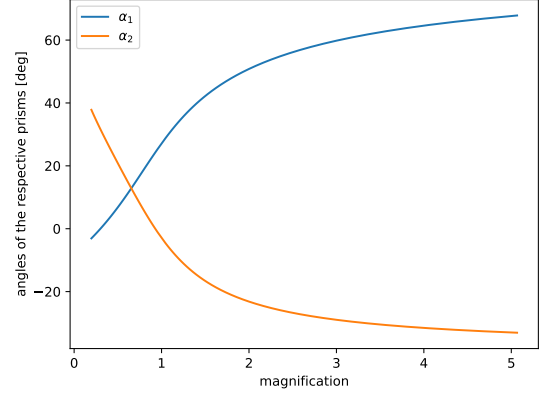
(b) Simulated magnification and corresponding prism angles. The constraint of parallel incoming and outgoing rays has been used for the calculation.

Figure 8: Results from a simulation of two anamorphic prisms with a wedge angle of 30°.

The angles α_1 and α_2 are defined as illustrated in figure 9. Since the angles in figure 8a are in both cases measured on the face of the prisms facing the parallel rays, the angle where the red line intersects the curve needs to be corrected by subtracting the wedge angle of the prism (30°) to obtain α_2. According to figure 8b a magnification of 1/3 requires the prisms to be mounted at the angles $\alpha_1 = 1.0°$ and $\alpha_2 = 29.8°$.
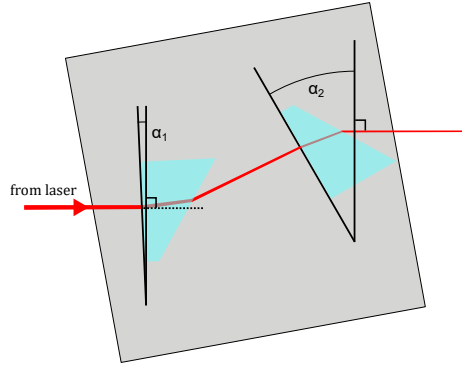

Figure 9: Schematic drawing of a pair of anamorphic prisms which are set at angles α_1 and α_2 to correct for the ellipticity of the laser beam.

2.3.5 Faraday isolator

Reflections from optics further down the optical path can seed unwanted modes into the laser system. To block these undesired reflections one can place an optical isolator behind the laser. Rayleigh has theorized an Faraday isolator built from two polarization filters and a Faraday rotator [30]. Such a Faraday isolator acts as an 'optical diode', letting laser light through in one direction and blocking unwanted reflections from reaching the other side.

2.3.6 Principle of self heterodyne linewidth measurement

Using a delayed self-heterodyne linewidth measurement setup the linewidth of the completed laser system can be determined. The laser beam enters the setup and gets split at a 50/50 beamcube (compare figure 10). One path will go through an acousto-optical modulator (AOM) which will increase the light's frequency by its input frequency when the first order output ray is used.

The other path passes through a delay line, which has in the existing setup been realized with a 10 km long fiber. The delay length L_{delay} must be greater then the correlation length of the laser, which is related to the coherence time $\tau_{\text{c}} = \frac{n_{\text{fiber}} \cdot L_{\text{delay}}}{c} \approx \frac{L_{\text{delay}}}{c}$. For long delays lines, where the delay time τ_0 is far greater than the correlation time of the laser τ_{c}, and the phases of the fields of the emitted light are uncorrelated. Therefore the power spectrum is expected to be Lorentzian with a width twice the FWHM of the laser spectrum [31]. To judge if the 10 km fiber has sufficient length the expected coherence length needs to be calculated with:

$$L_{\text{delay}} \gg c \cdot \tau_{\text{c}}. \tag{8}$$

The coherence time can be calculated from the linewidth Δf_{fwhm} of the laser using $\tau_{\text{c}} = \frac{1}{\pi \cdot \Delta f_{\text{FWHM}}}$ [32]. The two arms are combined with another 50/50 beamsplitter. To get a better signal-to-noise ratio the two beams should have the same intensity when combined, but passing through a 10 km fiber has attenuated the intensity of one arm. This is solved by controlling the polarization with a $\lambda/2$-plate in one path and placing a rotatable polarization dependent beam splitter (PBS) in the combined path. The $\lambda/2$-plate can be adjusted so that the polarization of the light originating from its path after the 50/50 beamsplitter is orthogonal to the polarization of the other part. The PBS can be rotated to select every ratio of these two beams, while the components in ray after the PBS also feature the same polarization direction.
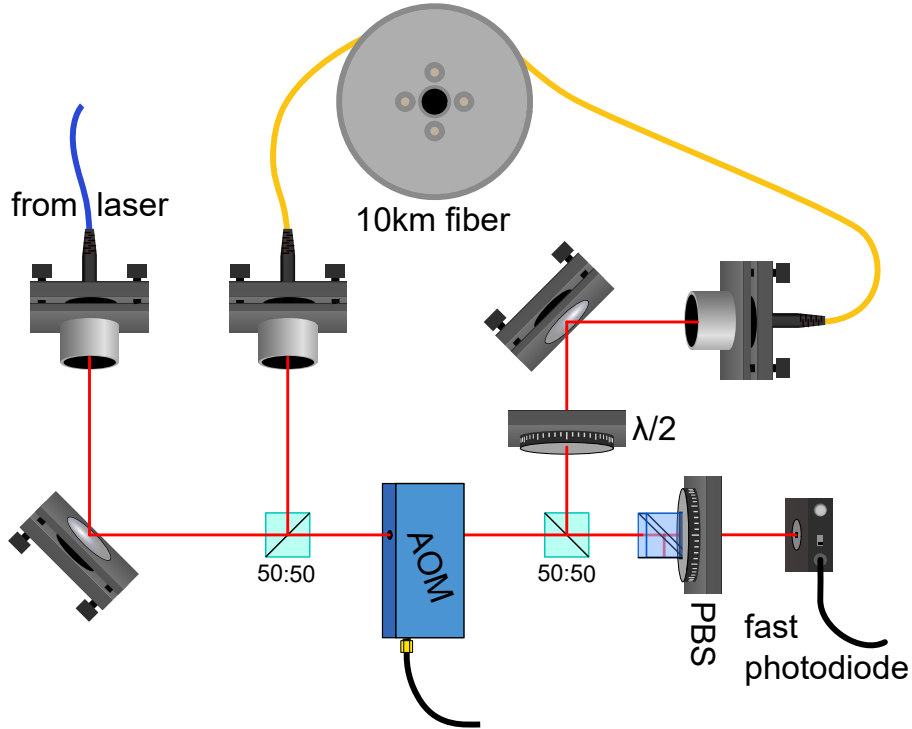

Figure 10: Schematic setup to measure the linewidth of the laser with a diffraction grating.

For now, consider the simplified case where the laser has an infinite correlation time and is

prefectly stable in frequency. The original laser's **E**-field then is given by:

$$\mathbf{E}_{\text{laser}} = \mathbf{E}_1 \cos(t \cdot 2\pi \cdot f_{\text{laser}}) \tag{9}$$

with $f_{\text{laser}} \approx 333\,\text{THz}$ in the case of a wavelength of $900.243\,\text{nm}$. The light in the first order of the AOM has a frequency shifted from f_{laser} by the driving signal's frequency of $f_{\text{AOM}} = 80\,\text{MHz}$:

$$\mathbf{E}_{\text{shifted}} = \mathbf{E}_2 \cos(t \cdot 2\pi \cdot f_{\text{shifted}}). \tag{10}$$

where $f_{\text{shifted}} = f_{\text{laser}} + f_{\text{AOM}}$.

The combined ray then hits a fast photodiode which must be fast enough to still capture frequencies close the AOM's frequency. In our simplified example the time delay does not affect the laser (appart from a constant phase offset which get's neglected here), so $\mathbf{E}_{\text{delayed}} = \mathbf{E}_{\text{laser}}$. The photodiode output voltage is as first approximation linearly dependent on the intensity and hence the square of the electric field amplitude [33]:

$$\begin{aligned} I_{\text{photodiode}} &= \left|\mathbf{E}_{\text{delayed}} + \mathbf{E}_{\text{shifted}}\right|^2 \\ &= \frac{1}{2}\left|\mathbf{E}_1\right|^2 \left(1 + \cos(t \cdot 4\pi f_{\text{laser}})\right) + \frac{1}{2}\left|\mathbf{E}_2\right|^2 \left(1 + \cos(t \cdot 4\pi f_{\text{shifted}})\right) \\ &\quad + \frac{1}{2} \cdot \mathbf{E}_1 \cdot \mathbf{E}_2 \cdot \left(\cos(t \cdot 2\pi(f_{\text{shifted}} + f_{\text{laser}})) + \cos(t \cdot 2\pi(f_{\text{shifted}} - f_{\text{laser}}))\right) \end{aligned} \tag{11}$$

Since the photodiode is not fast enough to respond to frequencies in the THz range only the term with the frequency $f_{\text{shifted}} - f_{\text{laser}} = f_{\text{AOM}}$ will be detectable on the oscilloscope which records the amplified photodiode voltage, which in our hypotetical case would be:

$$U_{\text{photodiode}} \approx \frac{1}{2} \cdot \mathbf{E}_1 \cdot \mathbf{E}_2 \cdot \cos(t \cdot 2\pi(f_{\text{shifted}} - f_{\text{laser}})) = \frac{1}{2} \cdot \mathbf{E}_1 \cdot \mathbf{E}_2 \cdot \cos(t \cdot 2\pi \cdot f_{\text{AOM}}). \tag{12}$$

Now let's consider the case of a finite correlation time which means the frequency is no longer constant in time: $f_{\text{laser}} \rightarrow f_{\text{laser}}(t)$. $\mathbf{E}_{\text{delayed}}$ will now depend on the delayed version of the frequency $f_{\text{laser}}(t + \tau_{\text{delayline}})$, where $\tau_{\text{delayline}}$ is the time the light takes to pass through the delay fiber. The photodiode sill is only able to detect the frequencies around f_{AOM} so equation 12 has to be modified to:

$$\begin{aligned} U_{\text{photodiode}} &\approx \frac{1}{2} \cdot \mathbf{E}_1 \cdot \mathbf{E}_2 \cdot \cos(t \cdot 2\pi(f_{\text{shifted}}(t) - f_{\text{laser}}(t + \tau_{\text{delayline}}))) \\ &\approx \frac{1}{2} \cdot \mathbf{E}_1 \cdot \mathbf{E}_2 \cdot \cos(t \cdot 2\pi((f_{\text{laser}}(t) + f_{\text{AOM}}) - (f_{\text{laser}}(t + \tau_{\text{delayline}})))) \end{aligned} \tag{13}$$

This means that the frequency fluctuations which determine the linewidth are now mixed into a range centered around f_{AOM}. Now the photodiode signal can be transformed into the freuqency domain with a fast Fourier transformation where a Voigt profile can be fitted to the data to determine the linewidth of the laser. The width of this FWHM of the Voigt profile is double the actual laser linewidth [33], since the autocorrelation between the Voigt peaks in frequency space of the laser and it's delayed signal lead to the final frequency distribution of $U_{\text{photodiode}}$. The FWHM for the Voigt-distribution can be approximated by

$$f_{\text{voigt,FWHM}} \approx 0.5246 f_{\text{lorentz}} + \sqrt{0.21166 f_{\text{lorentz}}^2 + f_{\text{gauss}}^2} \tag{14}$$

with $f_{\text{gauss}} = 2\sigma\sqrt{2 \cdot \ln(2)}$ and $f_{\text{lorentz}} = 2\gamma$ [34]. The resulting laser linewidth is:

$$\Delta f_{\text{laser,FWHM}} = \frac{\Delta f_{\text{Voigt,FWHM}}}{2} \tag{15}$$

2.4 Resonantor theory

To achieve the needed long term stability some way to measure the frequency drift of the laser is needed, to generate an error signal for compensation. For atoms such a stabilization can be realized with a spectroscopy lock [35], but the radical barium monofluoride does not exist in the gas phase and can therefore not be easily used in such a locking scheme. Therefore an optical resonator is used, the function principle of which is detailed in the following sections.

2.4.1 Construction of a Fabry-Pérot resonator

A Fabry-Pérot interferometer is an optical cavity between two reflective surfaces. When the cavity length is a multiple of the used wavelength the cavity will let most of the power pass through it. In a sense it is a frequency filter for light. By altering the mirror design or reflectivity the properties of the cavity can be modified so that the filtered frequency width gets narrower. There are multiple stable resonator designs with mirrors with different curvature [36]. The resonator type of the cavity which will be used in the following chapters is the hemispherical type with one spherical and on planar mirror (see figure 11).
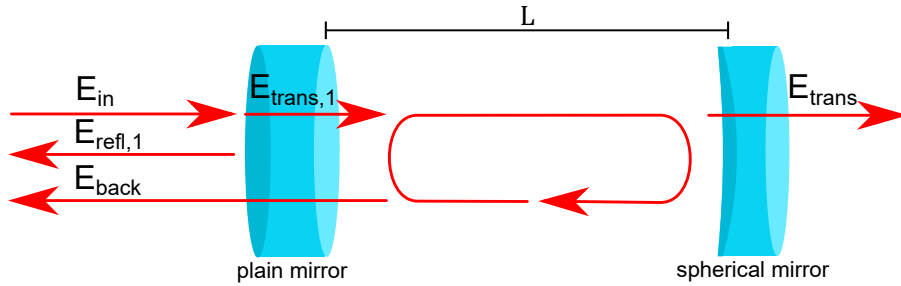

Figure 11: Electric fields inside the Fabry-Pérot cavity adapted from [37].

2.4.2 Free spectral range

The free spectral range Δf_{fsr} characterizes optical resonators and determines the frequency distance between adjacent primary modes in the frequency space. For a Fabry-Pérot cavity the free spectral range is determined by the distance between the mirrors L:

$$\Delta f_{\text{fsr}} = \frac{c}{n \cdot 2 \cdot L} \overset{\text{air}}{\approx} \frac{c}{2 \cdot L} \tag{16}$$

2.4.3 Finesse

The finesse $\mathcal{F}$ is a key indicator for the frequency resolution of an interferometer. At a fixed spectral range, a higher finesse means two lasers with smaller frequency differences can still be distinguished [38]. It is proportional to the number of interfering phasors and hence with the mean number of bounces inside a cavity. The number of bunces only depends on the reflectivity of the mirrors and their surface quality. According to [37] the Lorentzian finesse of a Fabry-Pérot resonator is given by:

$$\mathcal{F} = \frac{\Delta f_{\text{fsr}}}{\Delta f_{\text{fwhm}}} = \frac{2\pi}{-\ln(R_1 \cdot R_2)} \tag{17}$$

where Δf_{fwhm} is the frequency width of one transmission peak of the cavity and Δf_{fsr} is the distance between the peaks of the main cavity modes. R_1 and R_2 are the reflectivities of the two mirrors.

2.4.4 Large cavity

A $L = 1\,\text{m}$ long transfer cavity was built by [39] for a previous experiment in the same laboratory, and remains in use with the new laser cooling experiment. It is constructed in the symmetrical confocal configuration, using two spherical mirrors. Theoretical calculations by [39] predict a finesse of

$$\mathcal{F}_{\text{large}} = 313 \pm 141 \tag{18}$$

and a free spectral range of

$$\Delta f_{\text{large,fsr}} = 150 \pm 1.5\,\text{MHz or } \Delta f_{\text{large,fsr,degenerate}} = 75 \pm 0.75\,\text{MHz,} \tag{19}$$

depending on the mode matching, which can intentionally be misaligned to achieve a halfing in Δf_{fsr}. Since the error in length was not specified in the thesis of [39] an error of $1\,\text{cm}$ is assumed.

2.4.5 Tomschitz cavity

Another cavity was constructed in the Master's thesis of C. Tomschitz at the Institute [40]. It features one spherical and one planar mirror, just like the cavity in figure 11. This hermispherical design uses mirrors with a reflectivity of $(99.5 \pm 0.2)\,\%$. So the theoretical finesse of the Tomschitz cavity is, according to the calculations in chapter 2.4.3,

$$\mathcal{F}_{\text{tomsch}} = 627 \pm 251. \tag{20}$$

The length of the Tomschitz cavity is $L = 161.5 \pm 5\,\text{mm}$ [40], so using the equations in chapter 2.4.2 the free spectral range is calculated to be

$$\Delta f_{\text{tomsch,fsr}} = 928.2 \pm 29\,\text{MHz.} \tag{21}$$

An uncertainty in the exact length L of $\approx 5\,\text{mm}$ is assumed, because the mirror holder's positions are difficult to measure inside the lens tube and the position where the ray hits the curved surface of the back mirror is uncertain.

2.5 Laser locking with a digitallock

To stabilize a laser in its frequency one needs a way to precisely determine the frequency and frequency offset of the laser. Therefore a part of the laser's output power is used for the frequency stabilization. A resonator can be used to determine the current frequency of the laser or generating an error signal to correct for frequency fluctuations. With electronic feedback systems the laser can be influenced and fluctuations in frequency can be compensated.

2.5.1 Red Pitaya

The STEMlab 125-14, also referred to in short as the Red Pitaya is a hardware development platform built around the Xilinx Zynq 7010 FPGA. Two analog input channels can be sampled at $125\,\text{MS/s}$ and $14\,\text{bits}$ of resolution, and two $14\,\text{bits}$ digital to analog output channels can be used to generate arbitrary waveforms. Because it combines a programmable function generator with a mixer/demodulator a RedPitaya is well suited as a laser locking device.

One disadvantage of this solution is however, that the output voltage range of the RedPitaya is ranging only from $-1\,\text{V}$ to $1\,\text{V}$, while higher voltages would be required to drive the piezoelectric actuators of the cavities in use. Therefore two different amplifier circuits have been built, which are both detailed in chapter 5.

2.5.2 PID loops

Proportional-integral-derivative loops are the de-facto standard for stabilizing a system, as more than 90% of industrial controllers are implementations of the PID algorithm [41]. As the name implies the controller changes it's regulation output $o(t)$ proportionally to the difference of the current feedback value $i(t)$ to the setpoint s. Additionally the output is affected by the i-part which increases its influence if the error persists over a longer period. To compensate overshoot and counter instabilities the d-term takes the derivative of the feedback signal and adjusts the output based on the feedback's slope.

$$o(t) = K_p \cdot (i(t) - s) + K_i \int_0^t (i(t') - s)\, \mathrm{d}t' + K_d \cdot \frac{\mathrm{d}i(t)}{\mathrm{d}t}. \tag{22}$$

Depending on the response of the system to the output of the controller the parameters K_p, K_i and K_d in equation 22 can be adjusted to achieve faster stability around the setpoint.

When using digital logic to implement such a PID loop the data is sampled only at certain time steps. The integral part can be replaced by adding the current feedback value into a register, while the d-part is usually approximated by storing the last sample of the feedback and calculating the difference with the current feedback's value. If this should destabilize the output because of some delayed response of the controlled system advanced techniques like feeding the derivative therm's output through a low pass filter [42] or placing a low pass filter in front of the PID's input [43] can be deployed.

2.5.3 Pound-Drever-Hall technique for laser stabilization

The Pound-Drever-Hall-method, first presented in [44], makes it possible to create frequency error signals which are proportional to the frequency offset of the target laser's frequency. This error signal is usable in a feedback loop as described in chapter 2.5.2 to stabilize the laser against short and long term drifts. With this technique a laser can be stabilized with the reflected signal of a Fabry-Pérot cavity which is picked up by a photodiode.

The intensity of the reflected signal of a Fabry-Pérot cavity is given by the square of the sum of the electric field reflected off the first mirror before entering the cavity and the subsequent reflections from passes of the light inside the cavity [45]. The amplitude reflected electric field is given by [46]:

$$
\begin{aligned}
E_{\mathrm{refl}} &= E_{\mathrm{refl},1} + E_{\mathrm{back}} \\
&= -E_{\mathrm{in}} \cdot \sqrt{R} + E_{\mathrm{in}} \cdot T \cdot \sqrt{R}\, e^{2\pi i \frac{f_{\mathrm{lsr}}}{\Delta f_{\mathrm{fsr}}}} \sum_{m=0}^{\infty} \left(R \cdot e^{2\pi i \frac{f_{\mathrm{lsr}}}{\Delta f_{\mathrm{fsr}}}} \right)^m \\
&= -E_{\mathrm{in}} \cdot \sqrt{R} + E_{\mathrm{in}} \cdot T \cdot \sqrt{R} \left(e^{2\pi i \frac{f_{\mathrm{lsr}}}{\Delta f_{\mathrm{fsr}}}} \right) \frac{1}{1 - R \cdot \left(e^{2\pi i \frac{f_{\mathrm{lsr}}}{\Delta f_{\mathrm{fsr}}}} \right)} \\
&= -E_{\mathrm{in}} \cdot \sqrt{R}\, \frac{1 - (R+T) \cdot \left(e^{2\pi i \frac{f_{\mathrm{lsr}}}{\Delta f_{\mathrm{fsr}}}} \right)}{1 - R \cdot \left(e^{2\pi i \frac{f_{\mathrm{lsr}}}{\Delta f_{\mathrm{fsr}}}} \right)} = E_{\mathrm{in}} \cdot \sqrt{R}\, \frac{\left(e^{2\pi i \frac{f_{\mathrm{lsr}}}{\Delta f_{\mathrm{fsr}}}} \right) - 1}{1 - R \cdot \left(e^{2\pi i \frac{f_{\mathrm{lsr}}}{\Delta f_{\mathrm{fsr}}}} \right)}
\end{aligned}
\tag{23}
$$

where $R = 0.995$ is the reflectivity of the mirrors in the Tomschitz cavity and $T = 1 - R$ is the transmissivity. The sum over the reflections m is simplified using the geometric series. The reflected intensity which is plotted in figure 12 can be calculated with $P = E_{\mathrm{refl}} \cdot E_{\mathrm{refl}}^*$. The phase

of the transfer function is given by

$$F(f_{\text{laser}}) = \frac{E_{\text{refl}}}{E_{\text{in}}} = \sqrt{R} \frac{\left(e^{2\pi i \frac{f_{\text{lsr}}}{\Delta f_{\text{fsr}}}}\right) - 1}{1 - R \cdot \left(e^{2\pi i \frac{f_{\text{lsr}}}{\Delta f_{\text{fsr}}}}\right)} \tag{24}$$
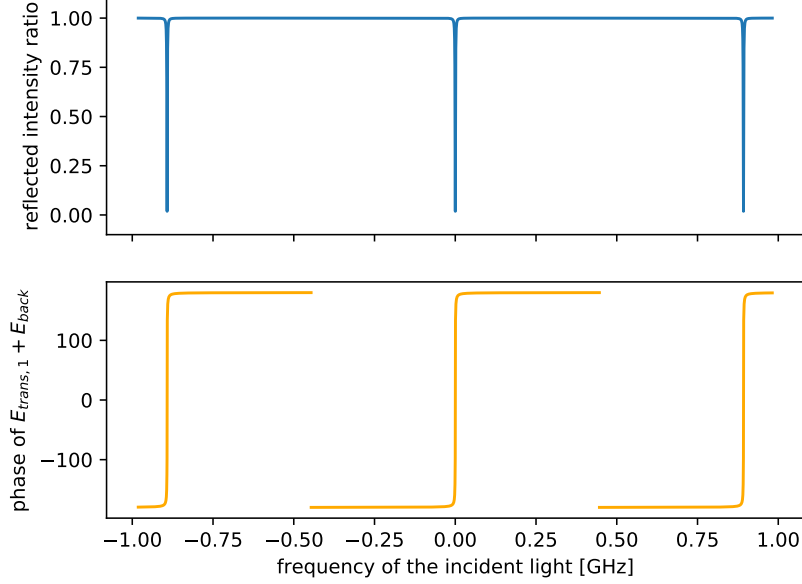
and is also graphed in figure 12.

Figure 12: Simulation of the intensity and phase of a cavity designed according to the properties in chapter 2.4.5, with the frequency of the incoming light being detuned from the point of resonance. The intensity dips periodically with $\Delta f_{\text{fsr}} = 928.2 \, \text{MHz}$. Phase and intensity can be calculated by summing the phasors of $\mathbf{E}_{\text{refl},1}$ and $\mathbf{E}_{\text{back}}$ [47]. Since $\mathbf{E}_{\text{refl},1}$ is reflected of the plain mirror it will pick up a phase of 180°.

The Red Pitaya generates sidebands on the laser with current modulation or with an EOM. When $\mathbf{E}_{\text{in}} = \mathbf{E}_0 \cdot e^{2\pi i f_{\text{lsr}} t}$ described the field before any modulation is applied, the electric field can now be approximated by [45]:

$$\mathbf{E}_{\text{in}} \approx \mathbf{E}_0 \left(J_0 \cdot e^{2\pi i f_{\text{lsr}} t} + J_1 \cdot \left(e^{2\pi i (f_{\text{lsr}} + f_{\text{mod}}) t} - e^{2\pi i (f_{\text{lsr}} - f_{\text{mod}}) t}\right)\right) \tag{25}$$

The radio of J_0 and J_1 depends on the depth of modulation. By transforming all three components with the transfer function $F(f)$, the power of the reflected signal can be shown to be [45]:

$$\begin{aligned} P_{\text{refl}} = {} & |J_0 \cdot F(f_{\text{lsr}})|^2 + |J_1 \cdot F(f_{\text{lsr}} + f_{\text{mod}})|^2 + |J_1 \cdot F(f_{\text{lsr}} - f_{\text{mod}})|^2 \\ & + 2 \cdot \sqrt{J_0^2 \cdot J_1^2} \left\{ \Re \left[F(f_{\text{lsr}}) \cdot F(f_{\text{lsr}} + f_{\text{mod}})^* - F(f_{\text{lsr}})^* \cdot F(f_{\text{lsr}} + f_{\text{mod}}) \right] \cos(2\pi f_{\text{mod}} t) \right. \\ & \left. + \Im \left[F(f_{\text{lsr}}) \cdot F(f_{\text{lsr}} + f_{\text{mod}})^* - F(f_{\text{lsr}})^* \cdot F(f_{\text{lsr}} + f_{\text{mod}}) \right] \sin(2\pi f_{\text{mod}} t) + \mathcal{O}(f_{\text{mod}}^2) \right\}. \end{aligned} \tag{26}$$

This reflected signal is picked up by a photodiode and demodulated in the Red Pitaya. The parts of equation 26 that oscillate with the light frequency are too fast to be picked up by the photodiode. By tuning the phase offset of the mixer we will be able to extract the sin term. The final error signal will hence be

$$\Im \left(F(f_{\text{lsr}}) \cdot F(f_{\text{lsr}} + f_{\text{mod}})^* - F(f_{\text{lsr}})^* \cdot F(f_{\text{lsr}} - f_{\text{mod}}) \right) \tag{27}$$

16

which is graphed in figure 13. This signal is asymmetric around the point where the maximum used to be in figure 12. Hence the laser can be stabilized independently of possible intensity fluctuations.
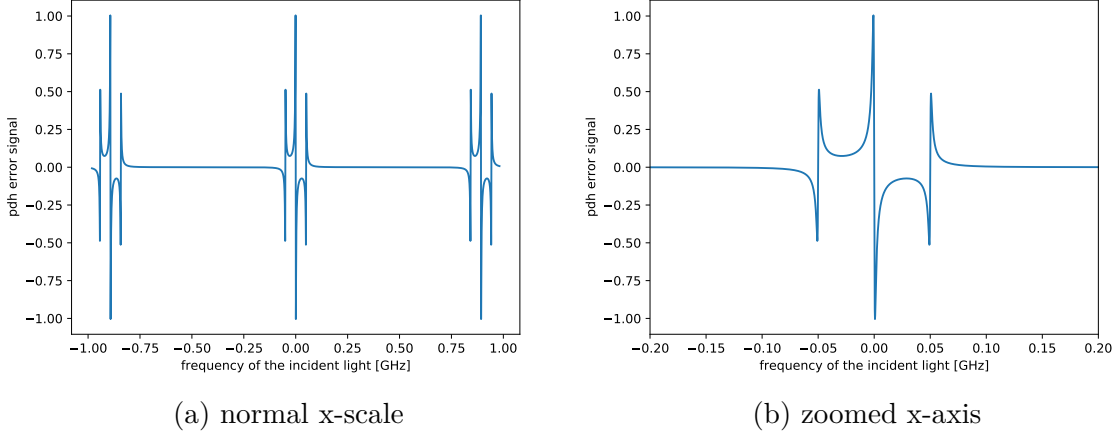

(a) normal x-scale

(b) zoomed x-axis

Figure 13: Error signal with sidebands of with a frequency of $f_{\mathrm{mod}} = 50\,\mathrm{MHz}$ on the zero crossing located at a frequency offset of $\Delta f = 0\,\mathrm{MHz}$. There is a steep slope at the frequency where the peak used to be. This region can be used to stabilize the laser.

An optionally filtered version of this signal is passed into a PID-controller which corrects the laser frequency by either tuning the grating angle or adjusting the DC laser current or a combination of the two. The complete schematic of all the parts needed for the PDH-lock can be found in figure 14.
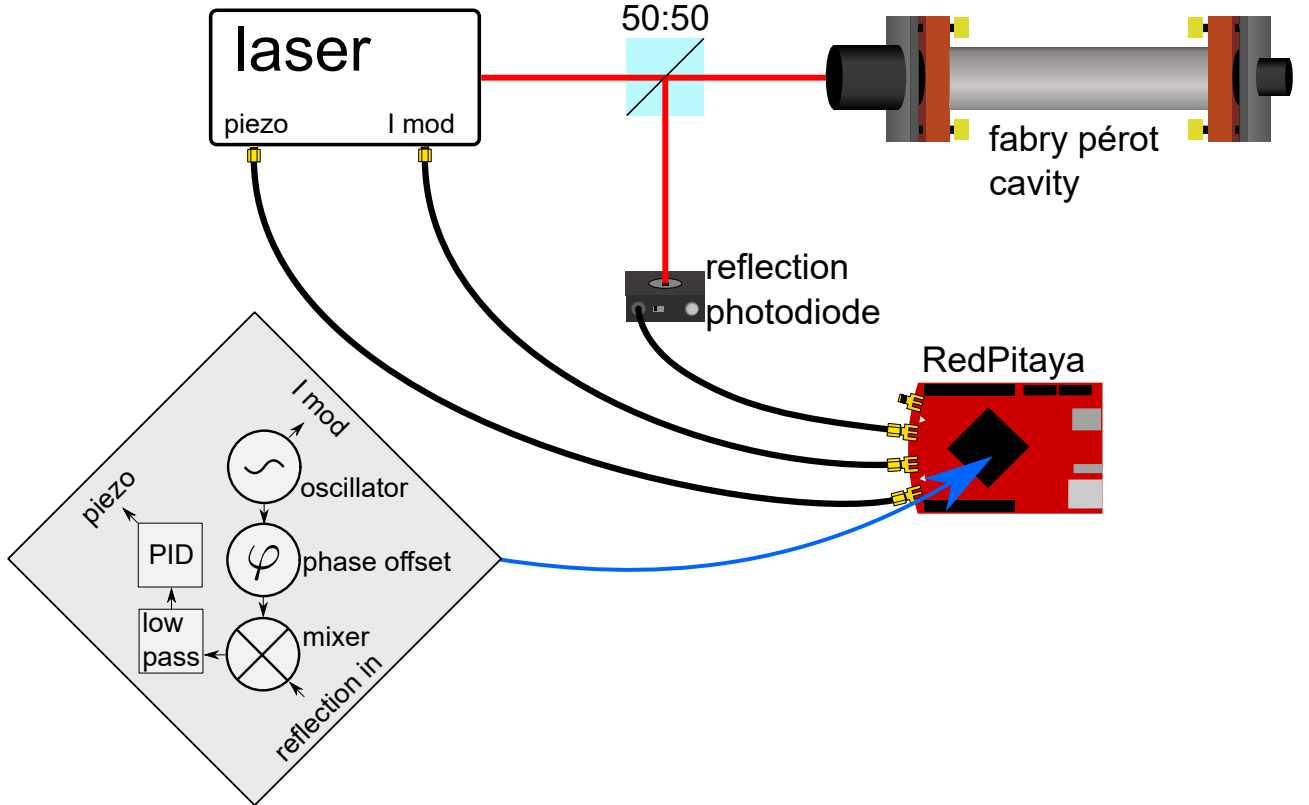
Figure 14: Schematic of the components of the Pound-Drever-Hall laser stabilization scheme inspired by [45]

3 Experimental Setup and Measurements

In this section, the construction of the laser system, the self heterodyne linewidth measurement setup, and the cavity setup for locking are described in detail. The laser system is characterized and locked on a fixed frequency.

3.1 Construction of the laser

To construct a suitable laser for use as a repumping laser as described in chapter 2.3.1 an existing design widely used at the 5th institute is adapted. The GaAs-semiconductor diode used is a LD-0910-0050-AR-1 Toptica photonics diode, with an antireflection and 40 mW rated output power. The diode is positioned inside a diode holder which itself contacts the base plate with thermal paste (see picture 15).

With the screws fixed at the diode holder the position of the lens block can be adjusted. By adjusting the aforementioned screws the direction of the outgoing beam is corrected so that it remains at constant height and perpendicular to the laser's housing. The lens block, made from nickel silver [48], can be moved along a plane perpendicular to the laser beam. The lens' distance to the diode can be adjusted by screwing it further into the lens block. This way the beam is collimated by simultaneously observing the change in radius of the beam with a detector card at a distance of roughly 7 m.

After passing this $f = 11$ mm lens, the beam then hits a 1200 lines/mm blazed grating in the Littrow configuration placed. The angle of this grating can be set with two fine adjustment screws, of which one is visible in this image. This screw pushes on a piezoelectric actuator which can be used to modulate or fine-tune the laser. The grating is initially positioned in an angle $\theta_{\text{litt}} = 32.69°$ as calculated in chapter 2.3.2.
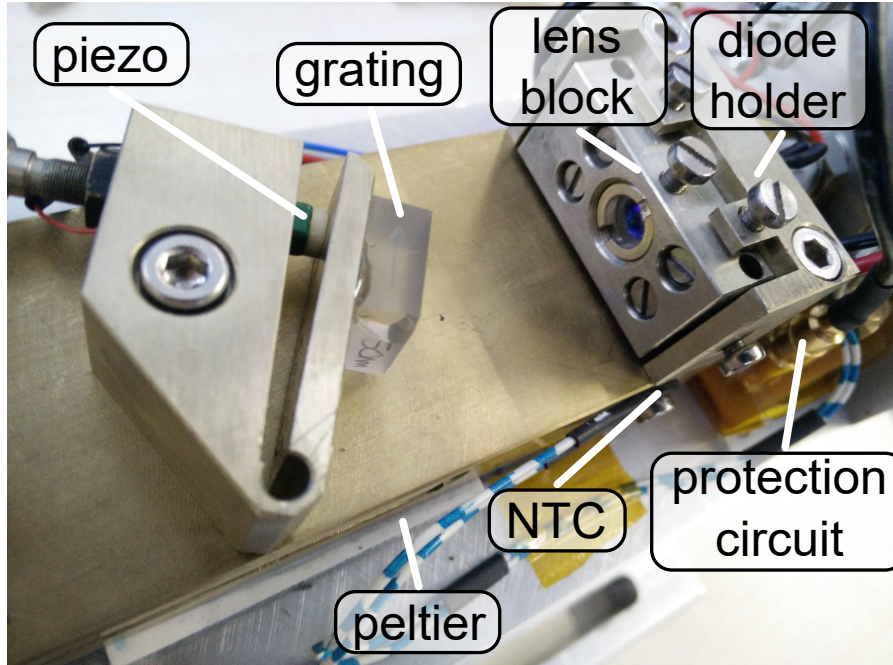

Figure 15: Photograph of the laser internals. The baseplate with the grating holder sits on a Peltier module. The temperature of the top assembly is measured with an NTC thermistor which acts as feedback for the thermoelectric cooler controller. The view to the diode is obscured by the adjustable lens block.

The beam ellipticity after the grating is corrected using an anamorphic prism pair, which is set up based on calculations in chapter 2.3.4 and measurement in chapter 3.3.
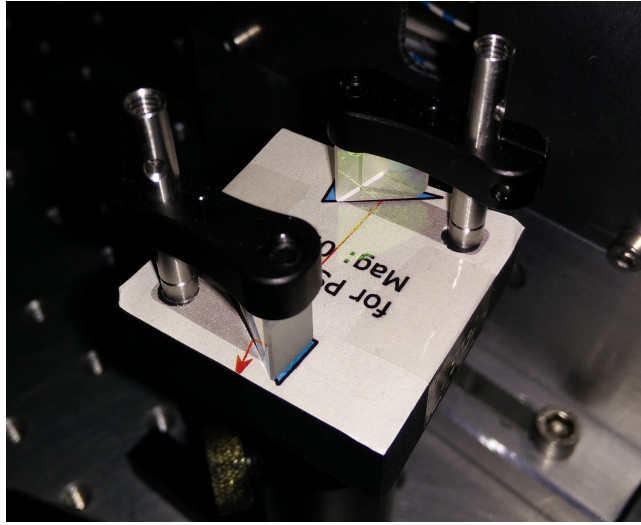

Figure 16: Anamorphic prism pair consisting of two Thorlabs PS871-B prisms with a wedge angle of 30° with an anti-reflection coating from 650 to 1050 nm. It is used to reduce the horizontal beam diameter increase caused by the emission profile of the laser diode.

Depending on the room temperature the baseplate would expand and contract based on the thermal expansion coefficient for brass $(19\,\text{°C}^{-1})$. Temperature variations of the diode would also lead to mode hops. To prevent both effects the top assembly is held at a constant temperature, which is achieved with a Peltier module sitting underneath the baseplate. A $10\,\text{k}\Omega$-NTC, which is screwed onto the side of the base, provides feedback for the temperature controller driving the Peltier. Thermal paste is used to improve the thermal contact between the thermoelectric cooler and the baseplate. The other side of the Peltier rests on a large aluminium block that acts as a heatsink.

3.2 Characterization of the laser diode

To measure the power an S121C power sensor from Thorlabs is placed in the collimated beam's path and the supplied diode current is varied while measuring the optical output power. With the recorded data in figure 17 the lasing threshold and relation between input current and optical output power are determined. Note, that this measurement is performed in absence of the grating.
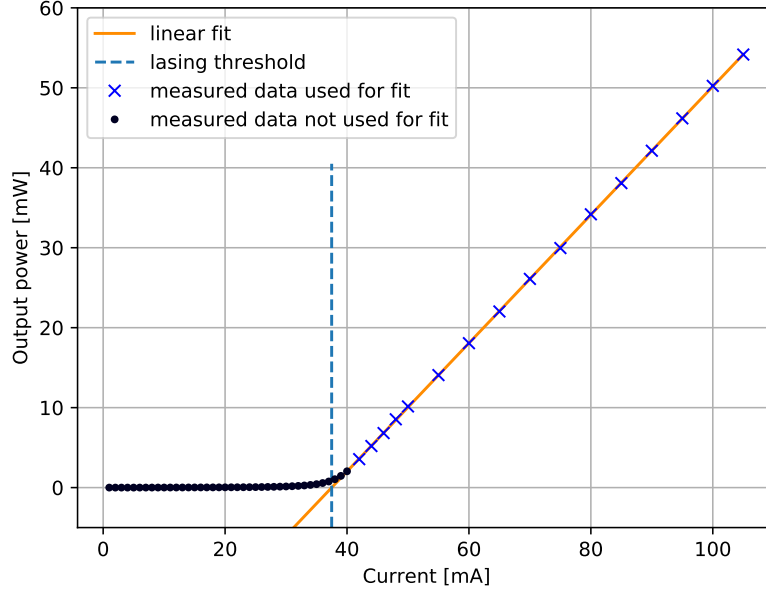

Figure 17: Power of the Toptica laser diode is measured while varying the supplied current. At $I_{\text{thresh,D}}$ = 37.483 mA the lasing threshold is reached and the stimulated emission starts to dominate the spontaneous emission. The laser power is increasing linearly with the supplied current. Therefore the parameters of the function $P(I)_{\text{stim,D}} = a_{0,\text{D}} \cdot I + b_{0,\text{D}}$ were determined from a least square fit including only the data points that clearly fall inside the stimulated emission regime. This yielded $a_{0,\text{D}}$ to be $0.802 \, \text{mW} \, \text{A}^{-1}$ and $b_{0,\text{D}} = -30.1 \, \text{mW}$.

Next, the beam's intensity profile is analyzed. Therefore an image of the collimated beam is recorded with a CCD-beam-profiler and illustrated in figure 18.
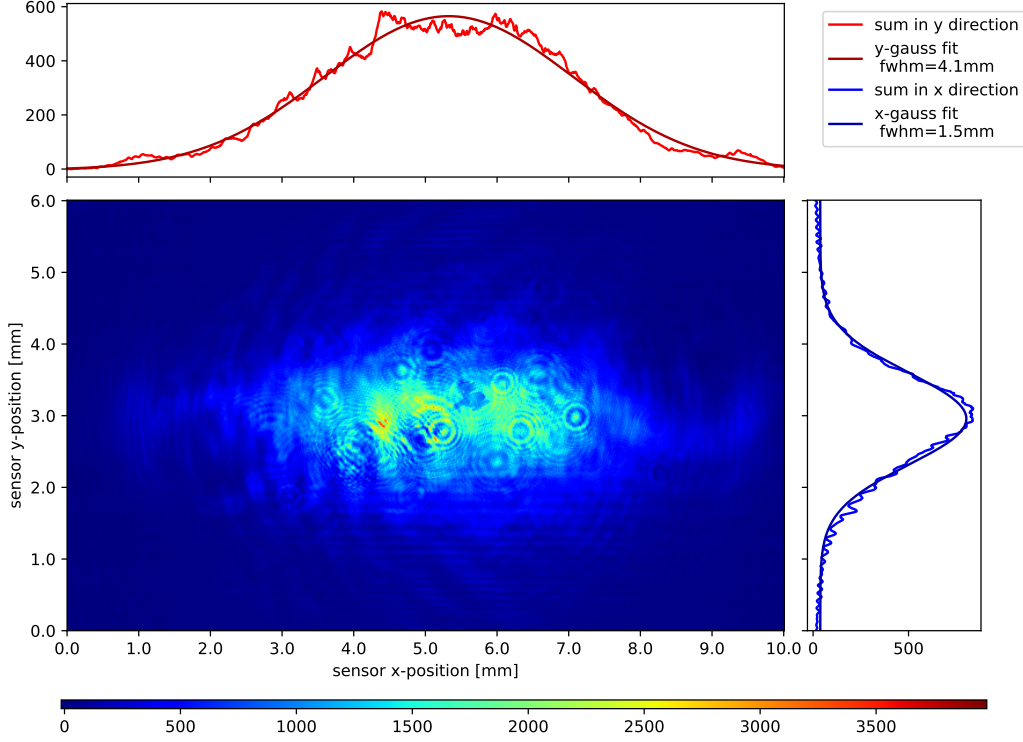
Figure 18: Intensity profile of the laser beam emitted from the Thorlabs diode in arbitrary units (intensity and pixels) as recorded using a Newport LBP2-VIS2 beam profiler. The CCD-data has been summed for each row and each column and has been divided by the number of pixels to arrive at the two histogram plots. To these samples a Gaussian is fitted with the method of least squares.

The profile is horizontally elliptical with a ratio of 2.48 : 1 which is typical for diode lasers [49]. Elliptical ratios vary from 2 : 1 to 4 : 1 which is caused by the rectangular cross-section of the emission aperture [50]. The emitted light is linearly polarized along the minor axis of the ellipse [49]. Since the intensity distribution in both axes does not show strong deviations from a Gaussian fit, it can be deduced that the emission is caused only by the TEM00 spatial-mode inside the lasing region [51].

3.3 Characterization of the laser with grating

To create a frequency tunable laser source as described in chapter 2.3 the -1st-order reflection of a blazed grating with 1200 lines/mm is aligned to hit the diode chip. By carefully adjusting the vertical and horizontal angle of the grating the Littrow configuration is achieved. Because the external resonator created by the grating induces stimulated emission in the laser's semiconductor chip the lasing threshold is reduced.

To identify the small set of angles where this lasing appears the diode current is set to a point close, but below the lasing threshold, in this case, 35 mA. When the reflected beam now overlaps perfectly with the outgoing beam the brightness and output power in the 0th diffraction order suddenly increases, since the diode is seeded by the external resonator. While searching and adjusting the horizontal and vertical angles of the grating the 0th order diffraction is projected onto a piece of paper, where the change in brightness can be observed with an infrared viewer.

After this point is found the output power is maximized with fine adjustment to the two setscrews.
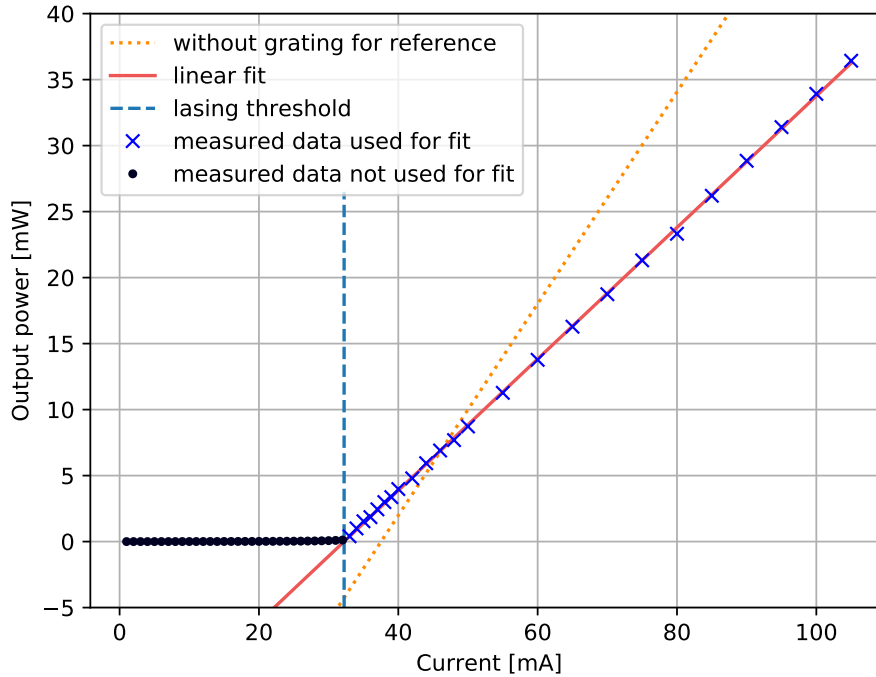
Figure 19: Power of the laser beam in the 0th diffraction order while varying the diode current. The fit function of figure 17 which approximates the output power in the stimulated emission region is added for comparison. The output power starts to increase at a lower current value compared to using only the diode.

The output power inside the 0th diffraction order is shown in figure 19 with the same setup as in 3.2.

Because of losses like absorption on the grating's surface or the power that goes into the other diffraction orders the obtainable output power is reduced for higher supplied currents (above 50 mA) when compared with the setup without the grating. As expected the stimulated emission occurs at a far lower current and hence the lasing threshold decreased from $I_{\mathrm{thresh,D}} = 37.5\,\mathrm{mA}$ to $I_{\mathrm{thresh,G}} = 32.2\,\mathrm{mA}$ in the Littrow configuration. The function $P(I)_{\mathrm{stim,G}} = a_{0,\mathrm{G}} \cdot I + b_{0,\mathrm{G}}$ has

again been fitted to the linear data region with the method of least squares. The resulting fit parameters are $a_{0,\mathrm{G}} = 0.498\,\mathrm{mW\,A^{-1}}$ and $b_{0,\mathrm{G}} = -16.0\,\mathrm{mW}$.

By slight modifications of the angle of the grating a wavelength selection can be achieved. The resonator inside the semiconductor chip can be stimulated to run in different modes and as the grating separates the arriving light by angle based on the wavelength, only selected wavelength will return into the lasing region.

To make these adjustments the laser's output is first passed through an optical isolator the principle of which is discussed in chapter 2.3.5. The beam is coupled into an optical fiber leading to a Advantest TQ8325 wavemeter which can be used to monitor the output wavelength while turning the horizontal adjustment screw slightly with a hex-wrench. With this setup the temperature-wavelength (figure 21) and current-wavelength (figure 20) dependencies are recorded to judge the stability of the laser.
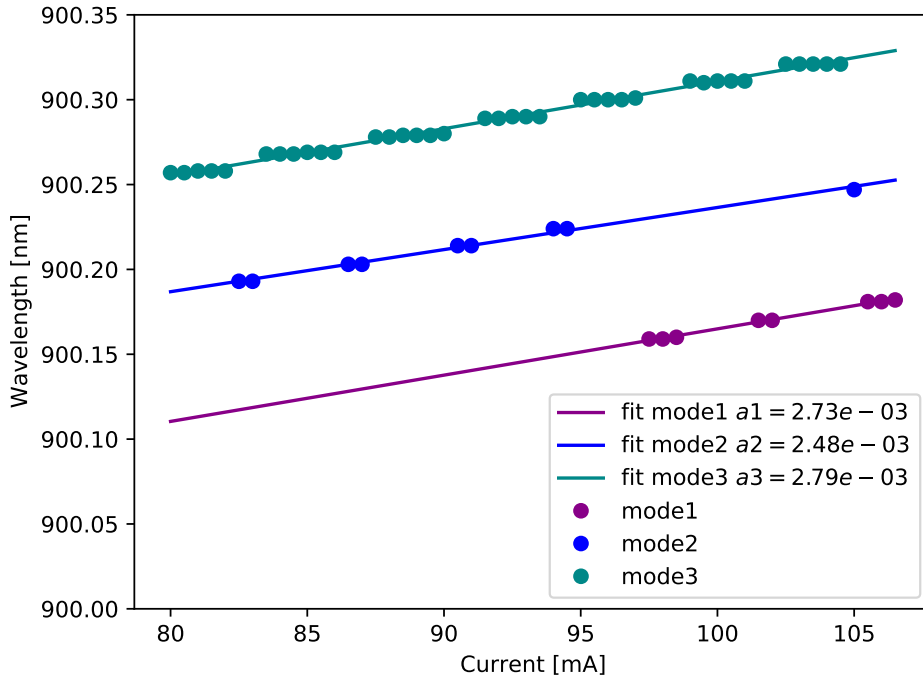
Figure 20: Measuring the wavelength vs the supplied current to the laser diode. The wavelength of the laser jumps between different modes which have a frequency difference of about 16.1 GHz. The data was sampled with the NTC-probe's resistance at $R_{\mathrm{NTC}} = 11.079\,\mathrm{k\Omega}$ which corresponds to a temperature of 22.71 °C.
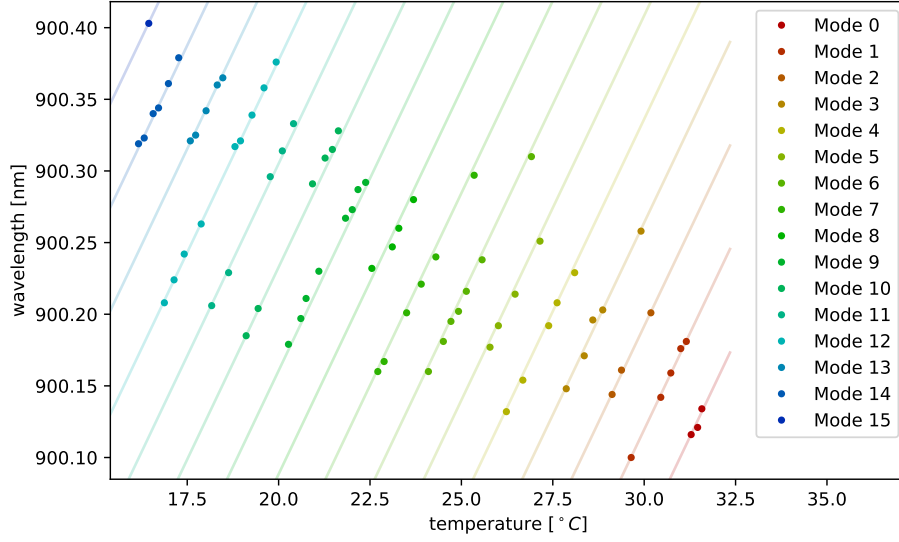
Figure 21: Measuring the wavelength vs the temperature of the laser assembly at a fixed diode current of $I_{\mathrm{D}} = 100.00\,\mathrm{mA}$. The modes are $26.7\,\mathrm{GHz}$ apart. The slope has been obtained by averaging over the slope of each mode. This results in a proportionality coefficient of $a = 19.9\,\mathrm{GHz\,K^{-1}}$.

The output ray in the 0th order of the grating is analyzed with the beamprofiler in figure 22. The ellipticity of the beam has increased from 2.48 : 1 to 3.2 : 1. This needs to be corrected by an anamorphic prism pair by the methods described in chapter 2.3.4.
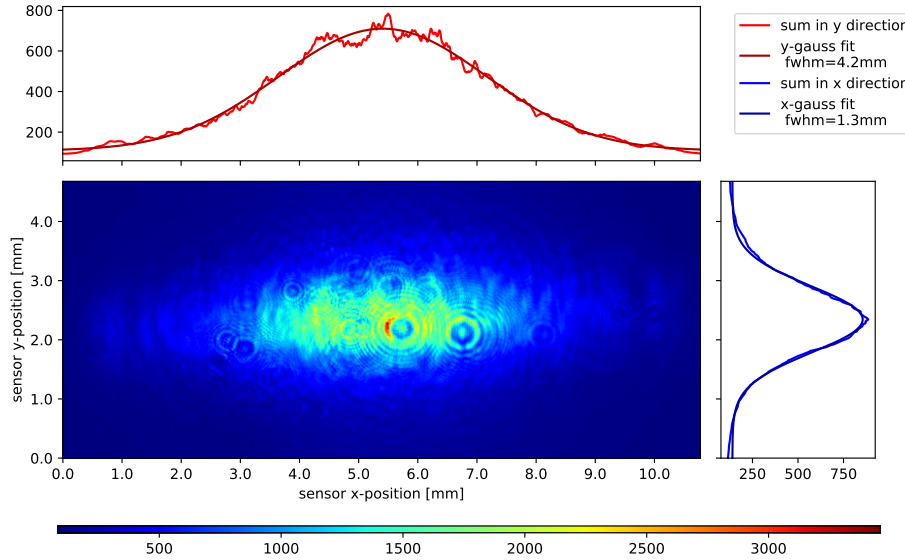
Figure 22: Beamprofile of the 0th-diffraction-order reflected by the grating. The ellipse has a ratio of 3.2 : 1.

The corrected beam is now slightly vertically elliptical, see figure 23. This is probably caused by a misplacement of one of the prisms or by the rotation of the complete prism holder.
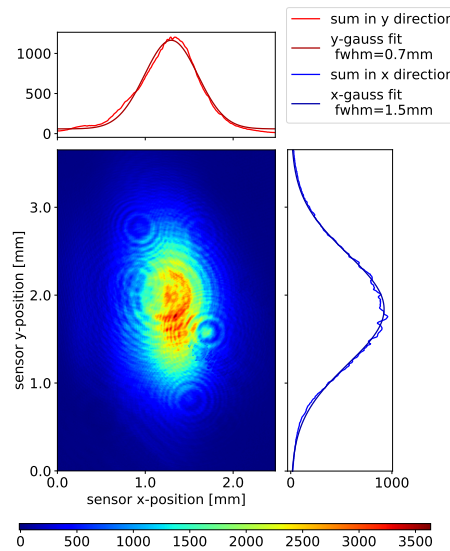
Figure 23: Beamprofile of the corrected beam behind the anamorphic prism pair. The resulting ratio is 1 : 2.1

3.4 Linewidth measurement

The measurement of the linewidth was performed according to the procedure detailed in chapter 2.3.6. With the smallest specified linewidth of the laser $\Delta f_{\mathrm{FWHM}} = 100\,\mathrm{kHz}$ the coherence time of the diode laser is according to chapter 2.3.6:

$$\tau_{\mathrm{c}} = \frac{1}{\pi \cdot \Delta f_{\mathrm{FWHM}}} = 3.18\,\mathrm{\mu s}. \tag{28}$$

The delay line must be therefore significantly longer than $l_{\mathrm{delay}} \gg c \cdot \tau_{\mathrm{c}} = 854\,\mathrm{m}$. Since our delay line is ten-times this length we expect the absence of periodical fluctuations in the self hetero-dyned signal [52], which is the case. The captured data from the photodiode was transformed with the fast Fourier transform and a Lorentz profile was fitted to the data obtained this way. Figure 24 shows the Voigt fit, from which the FWHM of the maximum was determined as

$$\Delta f_{\mathrm{voigt,FWHM}} \approx 942\,\mathrm{kHz}. \tag{29}$$

The laser linewidth then is half of this width:

$$\Delta f_{\mathrm{laser,FWHM}} = \frac{\Delta f_{\mathrm{voigt,FWHM}}}{2} = 471\,\mathrm{kHz}. \tag{30}$$

A width of less then $1\,\mathrm{MHz}$ is typical for external cavity diode lasers [53], so this result falls in the expected range.
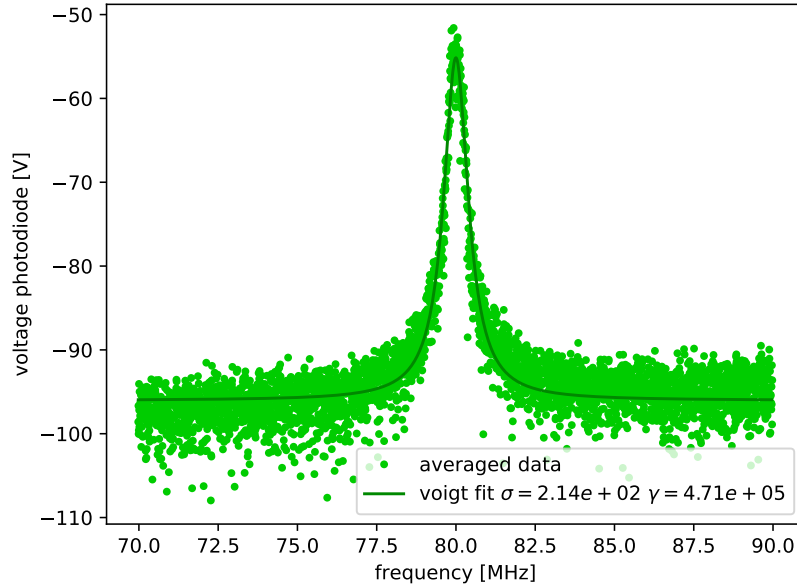

Figure 24: Fourier transformation of the measured photodiode voltage, which shows a maximum around 80 MHz.

3.5 Stabilisation with feedback from an external cavity

To counter long term drifting of the laser's frequency an external Fabry-Pérot interferometer can be used in conjunction with a stabilized master laser. As a temperature independent reference a master laser can be locked to a caesium D_2 line ($\lambda_{\mathrm{master}} = 852.347\,\mathrm{nm}$) from Doppler free spectroscopy inside a vapor cell. With this laser the compensation from drifts of the external

26

interferometer becomes possible and hence the newly build repump laser can be locked on this
stabilized cavity to achieve the long term stability needed for the experiment.

Because of problems with noise on one of the cavities a high finesse Fabry-Pérot cavity is
constructed and characterized (see chapter 2.4.5). This cavity is then used to stabilize the
main cooling laser by using it as a transfer cavity.

3.5.1 Setup of the Tomschitz cavity

The master laser and the laser that is going to be locked are overlayed and coupled into one
fiber. This fiber feeds into the cavity setup which is depicted in figure 25 and is labeled 'from
mixer'. An adjustable lens couples the light into the cavity. The retroreflected signal from the
cavity is separated from the incoming ray with a 50:50 beamsplitter and passed onto a fast
amplified photodiode (Thorlabs PDA10A). A small fraction of the transmitted ray is routed
into an USB camera to visually aid in the alignment process. The rest of the transmitted ray
hits another fast phodiode.

The Fabry-Pérot cavity itself has a fixed spherical mirror on one end with a focus distance
$f_{\text{spherical}} = 200\,\text{mm}$. The front planar mirror is glued onto a piezo stack which has a hole in the
middle so the ray can pass through it. By applying a voltage on the piezo-stack the length of
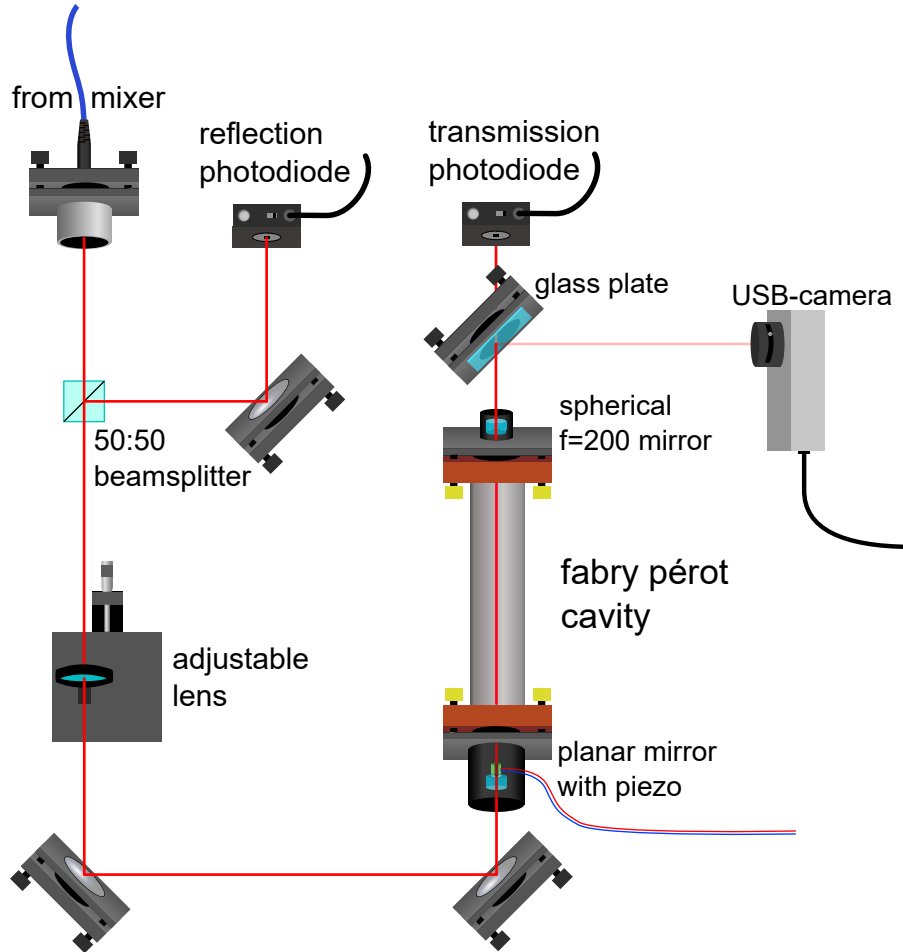the cavity can be scanned in the µm range.

Figure 25: Schematic drawing of the optical Fabry-Pérot cavity setup

The initial alignment is done by removing both mirrors and replacing them with an iris aperture.

The diameter of the iris hole is iteratively reduced while adjusting the path of the ray with the two mirrors in front of the cavity, so that the ray is still visible on a detector card placed at the exit of the cavity. After the initial alignment the mirrors were screwed back on and the cavity is continuously scanned with a ramp with $V_{pp} = 10\,$V. With the help of the live picture of the USB camera the reflections of the two mirrors were overlayed by rotating the fine adjustment screws of both mirror holders. The camera shows an overlayed picture, which is created by the reflection on the front and back face of the glass plate, but for adjusting the positions of the mirros this image is sufficient. When placing the camera directly into the beam path without a glass plate and slowly scanning the piezo different cavity modes can be observerd depending on the alignment. For a well aligned cavity the cylindrical TEM modes in figure 26 are visible. When the alignment is off in the horizontal direction (simulated by turning the back spherical mirror out of alignment in figure 27) the rectangular TEM modes are visible.

(a) TEM00 mode   (b) TEM10 mode   (c) TEM20 mode
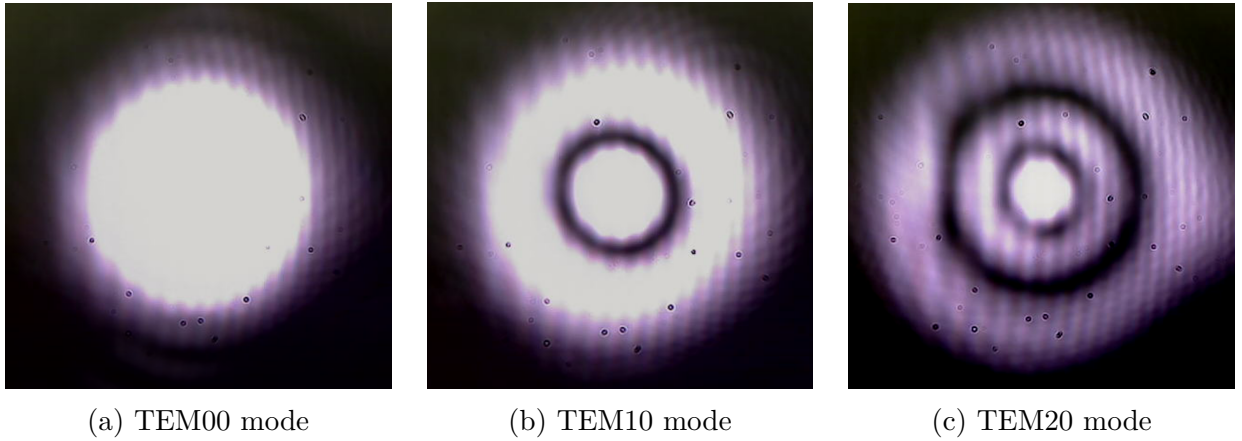
Figure 26: Cylindrical TEM modes of a well aligned cavity recorded with a camera behind the cavity. The small black dots are caused by particles on the camera's sensor.

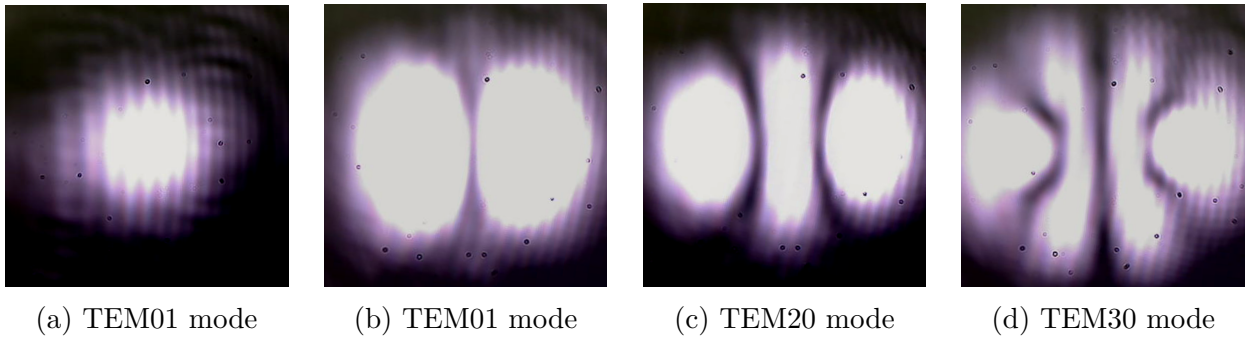(a) TEM01 mode   (b) TEM01 mode   (c) TEM20 mode   (d) TEM30 mode

Figure 27: Rectangular TEM modes of a cavity where the back mirror of the cavity is rotated horizontally out of alignment. The small black dots are again caused by particles on the camera sensor.

3.5.2 Large cavity characterization

In order to have a fair comparison of the noise signals on the reflection signal of both cavities, the relation between piezo scan voltage and scanned frequency must be determined. For this purpose Δf_{fsr} and the finesse of the large cavity is measured and later used to scale the x-axis in figure 32. By scanning the cavity with the Caesium laser with a wavelength of $\lambda_{\text{Cs}} = 852.347\,\text{nm}$ with modulated sidebands of $f_{\text{mod}} = 20\,\text{MHz}$ the free spectral range can be calculated. The measured data for this calculation can be found in figure 28.
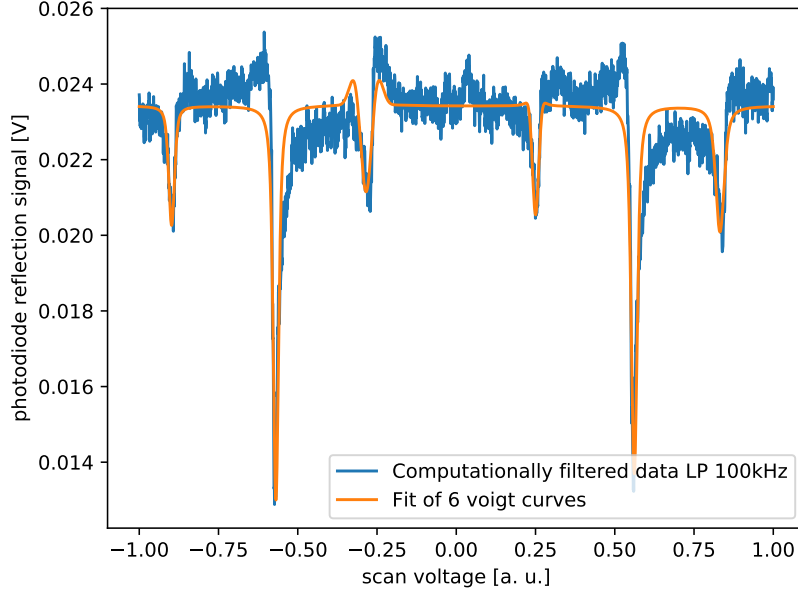
Figure 28: Scan of the large cavity of a laser with modulated sidebands on the Caesium laser. The measured data is electronically filtered with a low pass filter with a cutoff frequency of $f_{\text{LP}} = 100\,\text{kHz}$ and cropped so that exactly two main modes with their sidebands are visible.

By fitting Voigt profiles to these samples and calculating the distances of their respective centers the free spectral range can be obtained by

$$\Delta f_{\text{large,fsr,measured}} = \frac{\Delta U_{\text{main modes}}}{\Delta U_{\text{main mode to sideband}}} \cdot f_{\text{mod}} = \frac{1.130}{0.300} \cdot 20\,\text{MHz} = 75.7\,\text{MHz}. \tag{31}$$

This matches with the predicted error of the degenerate free spectral range $\Delta f_{\text{large,fsr,degenerate}} = 75 \pm 0.75\,\text{MHz}$ from chapter 2.4.4 reasonably quite well.

The measured finesse with the data from figure 29a is

$$\mathcal{F}_{\text{large,measured}} = \frac{\Delta U_{\text{main modes}}}{\Delta U_{\text{FWHM}}} = \frac{\Delta f_{\text{fsr}}}{\Delta f_{\text{FWHM}}} = 83.5 \pm 23. \tag{32}$$

The disparity might be caused by the noise on the signal, in figure 29a one can clearly see that the dip-width ΔU_{FWHM} is different for the left and right dip because of the noise. Therefore the measured finesse is derived by averaging the fitted width of the two dips. For the error the deviation from the mean width of both peaks is used in combination with linear propagation of uncertainty. Still, a large discrepancy exceeding the respective error range remains between the expected and measured values for the measured finesse of this cavity and the theoretical predictions from chapter 2.4.4. The source of this discrepancy remains unclear. Its magnitude is highlighted in figure 29b, which shows a comparison of one of the right measured dip with the corresponding much narrower theoretically expected line shape, visualized as green shaded area.

An additional information we can obtain from figure 29a is the voltage needed to scan $f_{\text{large,fsr}}$:

$$U_{\text{large,fsr}} = 5.63 \,\text{V} \tag{33}$$

which will be used to scale figure 32.

(a) full scan range

(b) zoomed in version of the right dip to show allowed peakwidths for range of finesse values
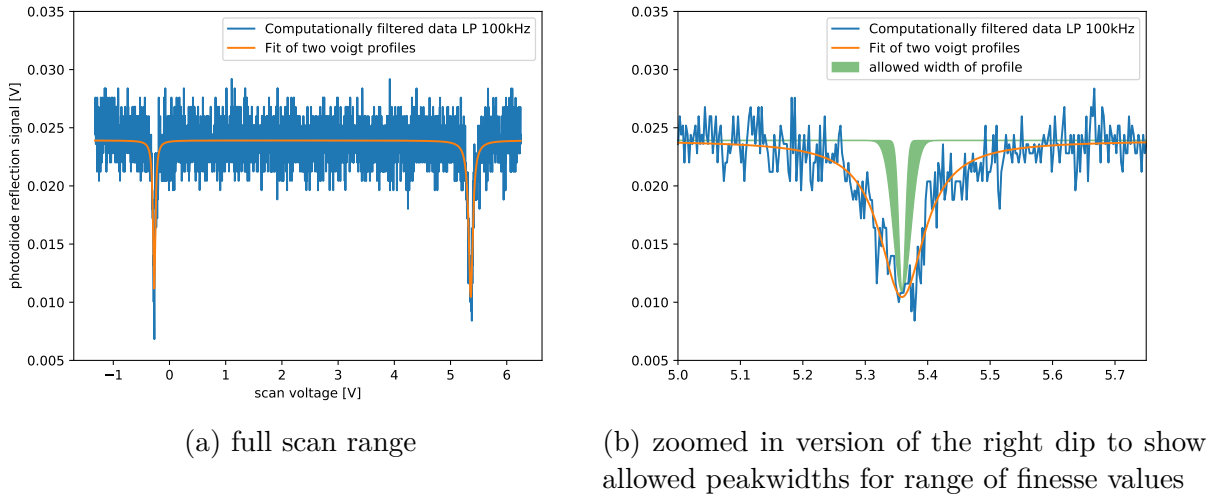
Figure 29: Scan of the large cavity of a laser of the wavelength $\lambda = 852.347\,\text{nm}$ laser.

3.5.3 Tomschitz cavity characterization

In this chapter the actual free spectral range and finesse of the Tomschitz cavity is measured and compared to the predictions in chapter 2.4.5.
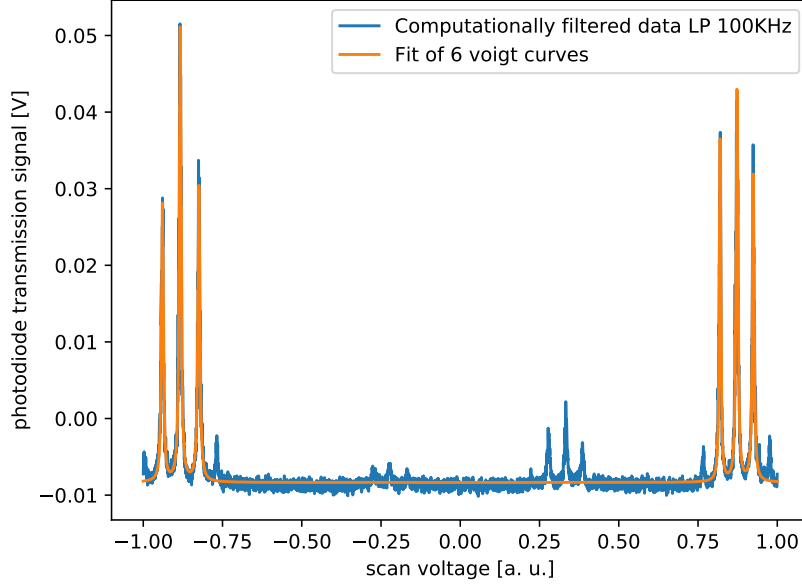

Figure 30: Scan of the tomschitz cavity of a laser with modulated sidebands with a modulation frequency $f_{\mathrm{mod}} = 30\,\mathrm{MHz}$.

To find $\Delta f_{\mathrm{tomsch,fsr}}$ of the cavity the supply current of the main cooling laser is modulated and coupled directly into the Tomschitz cavity setup. The modulation frequency used is $f_{\mathrm{mod}} = 30\,\mathrm{MHz}$ and the transmission photodiode's signal is depicted in figure 30.
To derive the free spectral range from this graph, the distance between the two main modes $\Delta U_{\mathrm{main\ modes}}$ and the distance of one side peak to the corresponding main mode's peak $\Delta U_{\mathrm{main\ mode\ to\ sideband}}$ is calculated. These distances are related to the free spectral range with:

$$\Delta f_{\mathrm{tomsch,fsr,measured}} = \frac{\Delta U_{\mathrm{main\ modes}}}{\Delta U_{\mathrm{main\ mode\ to\ sideband}}} \cdot f_{\mathrm{mod}} = \frac{1.7565}{0.0549} \cdot 30\,\mathrm{MHz} = 959.3\,\mathrm{MHz}. \qquad (34)$$

This measured value is +3.4% above the calculated $f_{\mathrm{tomsch,fsr,calculated}} = 928.2\,\mathrm{MHz}$ taken from chapter 2.4.5. One possible cause for this could be a wrong measurement of the cavity's length leading to a wrong predicted Δf_{fsr}. The distance of the mirrors could not exactly be measured since they are recessed into lens holders. Another possibility is that both mirrors are misaligned by the same angle, leading to the same optical characteristics but a slightly larger cavity length due to the construction of the mirror holders.
As a second step in the characterization the scan voltage to scan over Δf_{fsr} is extracted from the data in figure 31.
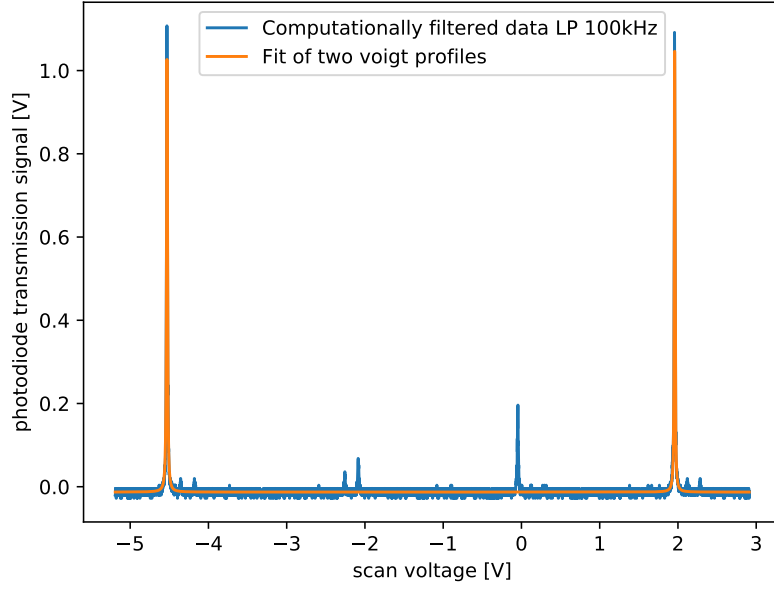
Figure 31: Scan of the tomschitz cavity with a 852.347 nm laser. The measured data is cropped so that exactly two main modes with their sidebands are visible.

The two fitted Voigt functions have a scan voltage offset corresponding to the voltage needed to scan the free spectral range of

$$\Delta U_{\text{tomsch,fsr}} = 6.49\,\text{V}. \tag{35}$$

The average full width half maximum of both Voigt functions is calculated with equation 14 and turns out to be $\Delta U_{\text{FWHM}} = 0.0129 \pm 0.0013\,\text{V}$. The error was derived the same way as in chapter 3.5.2, by calculating the distance from the mean peak width. This results in a finesse of:

$$\mathcal{F}_{\text{tomsch,measured}} = \frac{\Delta f_{\text{fsr}}}{\Delta f_{\text{FWHM}}} = \frac{957.6\,\text{MHz}}{2.42 \pm 0.25\,\text{MHz}} = 503 \pm 48 \tag{36}$$

which is 20% below the maxium achievable finesse from chapter 2.4.5.

3.5.4 Noise comparison

The distorted reflection signal of the large cavity (see figure 32) was the reason to build and characterize the new Fabry-Pérot cavity, designed by Tomschitz. In this chapter the noise of the reflection signals of both cavities is compared.

The dip in the reflection signal of this cavity is less noisy and the signal to noise ratio is better, even with 1/10 the input power. Another possibility would be that the large cavity is susceptible to vibrations originating from the vacuum pumps. The large cavity is suspended below the experimental table on a separate breadboard underneath the main optical table. The Tomschitz cavity's noise performance was tested in two locations. First it was placed on a small undampened side table, and was later moved onto the main optical table. This should positively affect the signal to noise ratio, since vibrations from the pumps will get dampened by the feet of the optical table.
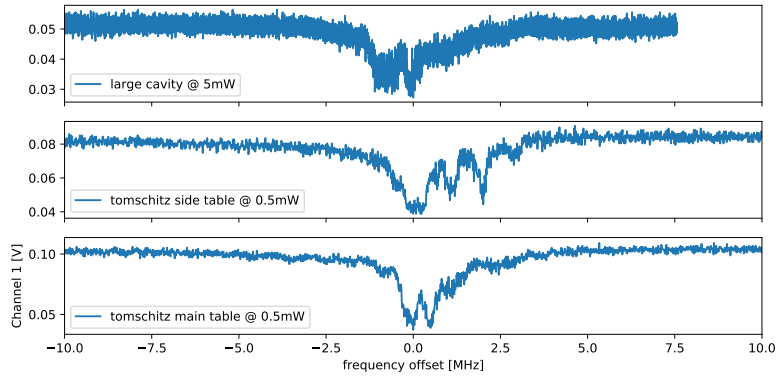
Figure 32: Comparison between reflection signals of different cavity setups.

In the Fourier transformed data (figure 33) is is obvious, that the large cavity exhibits more noise dips, compared to the Tomschitz cavity. The setup where the Tomschitz cavity is on the table has improved noise characteristics when compared to the placement on the separate undampened table.
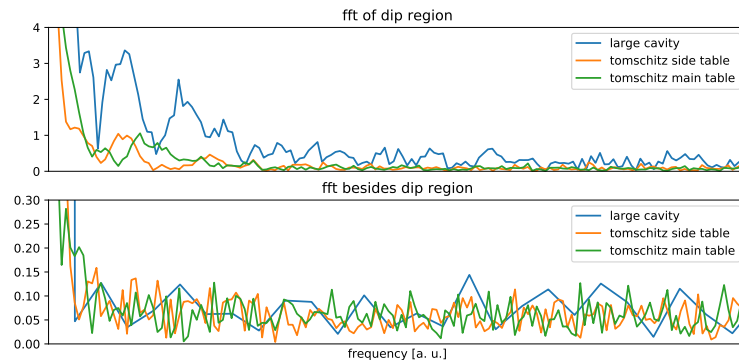
Figure 33: Fourier transformation of the signal from figure 32. The Fourier transformation of the data in close proximity to the dip is plotted in the upper part, while the Fourier transformation of samples away from the peak are graphed in the lower half. The frequency axis is given in arbitrary units since the original x-Axis in figure 32 is rescaled differently for the large- and the Tomschitz cavity, since their free spectral ranges differ.

3.5.5 Tomschitz cavity piezo non-linearity

In this part the non-linear response of the piezo stack inside the Tomschitz cavity is characterized. With the parameters obtained in this section a potential non-linearity can be corrected. The Red Pitaya scans the cavity and aquires the photodiode's transmission signal. Calculation of the positions of the main modes are performed with this signal. Simultaneously the laser that is used for this characterization is shifted in frequency by altering the voltage applied to the grating controlling piezo U_{grat}.

The non-linearity measurement is automated and consists of the following sequence of steps:

1. While the laser's grating is kept at a fixed voltage $U_{\text{grat}} = 0\,\text{V}$. Meanwhile the cavity is scanned, which results in a graph like figure 34. The peaks are labeled with ascending integers for ascending scan voltage and their position on the x-axis is stored for the next steps.

2. A small offset voltage is applied to the grating piezo in the laser. The cavity is scanned once again, but this time the positions of the maxima has shifted slightly to the left or to the right, thanks to the altered frequency of the laser. By comparing the positions of the peaks with the results first step their movement direction can be determined.

3. The offset voltage needed to shift the peaks by one index needs to be determined. The cavity is still scanned. The grating peaks are moved to the positions where their neighboring peak used to be, by iterative adjustment of the grating voltage. The voltage obtained in this step will be labeled $U_{\text{grat,scanrange}}$.

4. To sample the piezos non-linearity on more points than the three peaks occuring in the first step the peaks the voltage of the grating is varied stepwise beginning from $U_{\text{grat,start}} = -\frac{U_{\text{grat,scanrange}}}{2}$ until U_{grat} reaches $U_{\text{grat,end}} = \frac{U_{\text{grat,scanrange}}}{2}$. Along the way the cavity is scanned and the positions of the peaks are recorded. The grating voltage is varied in 200 steps and for every label of the maximas is changed to a new floating point number according to:

$$\text{label} = \text{number of mode} + \frac{\text{current iteration step}}{200}. \tag{37}$$

This labeling makes sense, because when the first peak has reached the previous position of his neighboring second peak it is now accurately referred to as the peak with the label 2.0.

When there is a new peak entering the side scan area the numbering is adjusted so that the peaks retain their number. The data obtained by such an run can be seen in figure 35. Every scan step adds as many points to the plot as there are maxima in the scan range.

5. As last step the polynomial

$$f(x) = a_0 \cdot x^3 + b_0 \cdot x^2 + c_0 \cdot x + d_0 \tag{38}$$

is fitted to the obtained data, where the x-axis is the peak's label and the y-axis it the peaks scan voltage offset, where it appeared.
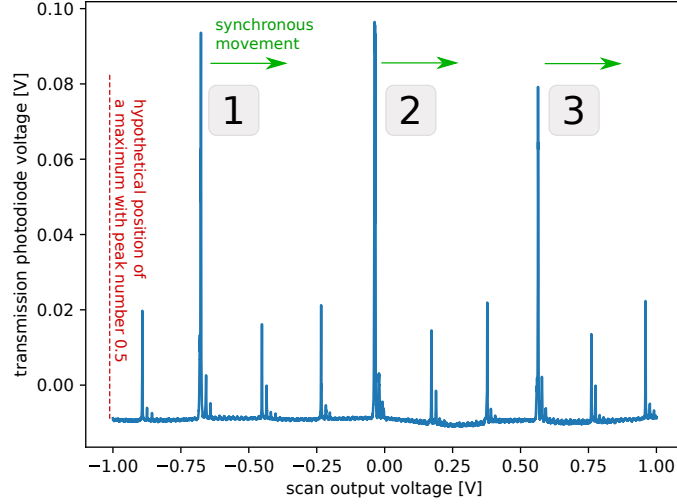
Figure 34: Scanning the Fabry-Pérot cavity with the Red Pitaya. The scan voltage is amplified with the non inverting operational amplifier rack module to have at least three peaks visible at any time. For this scan $U_{\mathrm{grating}} = 0\,\mathrm{V}$.

The fit parameters for the curve depicted in figure 35 are $a_0 = 0.0039$, $b_0 = -0.0349$, $c_0 = 0.6929$ and $d_0 = -0.9627$. At x-values close to integer numbers there are mode data points which had to be discarded. This is probably an area where a new maximum has entered from the left, but was not correctly recognized. Additionally the data between these integer values is bent upwards. This is a result of the temperature drift of the cavity during the measurement which takes about 5 minutes. A better thermal isolation or faster scanning would lessen the effect.
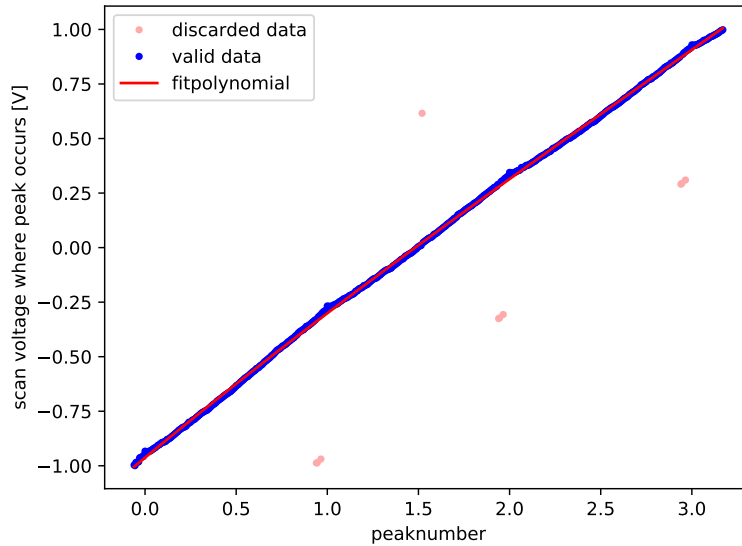
Figure 35: Peak positions when scanning the cavity while altering the wavelength of the laser to improve coverage of piezo positions. With this data the function to invert the piezo's non-linearity can be obtained.

The piezo behaves almost linearly for the voltage range, which can be produced by the amplifier boards. A correction of the non-linearity is therefore not necessary.

3.5.6 Long-term stability over time

To judge the long-term drift of the cavity due to temperature fluctuations the locked master laser is fed into the cavity while the cavity is continuously scanned. Due to slight temperature drifts the length of the cavity does change slightly which shifts the minima of the reflected signal to a different piezo voltage. By logging the voltage where the peaks occur over time the change in frequency as follows:

$$\Delta f = \frac{U_{\text{current minimum}} - U_{\text{first minimum}}}{\Delta U_{\text{two minima}}} \cdot \Delta f_{\text{tomsch,fsr}}. \tag{39}$$

The drift over the course of roughly one hour is graphed in figure 36.
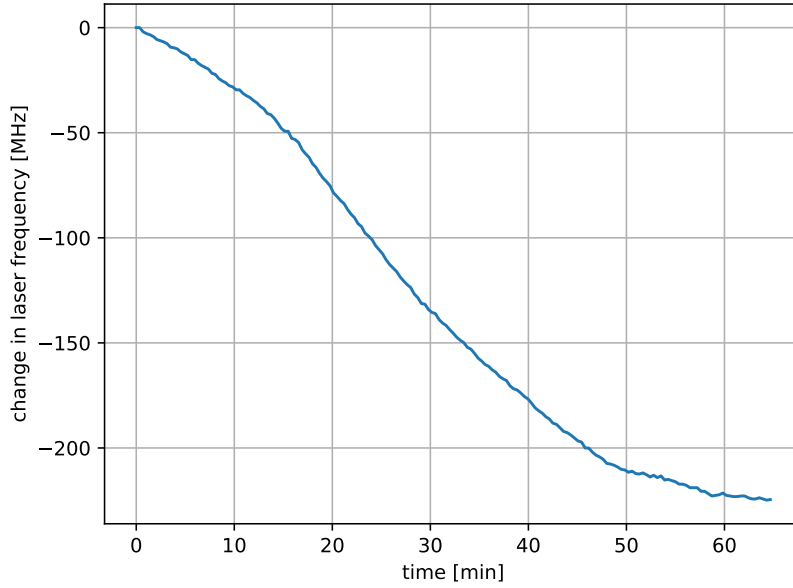
Figure 36: Drift of the cavity's reported frequency offset of a locked caseium laser, caused by a temperature induced change in mirror distance inside the cavity.

The tube of the cavity is manufactured from stainless steel which has a temperature expansion coefficient of $\alpha = 17.2 \cdot 10^{-6}$ K^{-1} [54]. For a cavity length of $l = 161.5$ mm this would mean that the temperature of the cavity has changed by $|\Delta T| = \frac{|\Delta l|}{l_0 \cdot \alpha} = 0.07$ K over one hour. This drift corresponds to a frequency shift of $\Delta f = 220$ MHz which needs to be compensated. As a comparison, the linewidths of the transitions used for cooling are in the order of a few MHz. The big drift in temperature would result in the laser's wavelength moving out of resonance with these transitions.

3.5.7 Locking with linien

In following the setup for locking the laser system is presented. It grants the possibility to compensate for the temperature induced frequency offsets of the transfer cavity, as discussed in chapter 3.5.6. To simplify the example the repump lasers are omitted but can be locked analogously to the main cooling laser.

The master laser at $\lambda = 852.347$ nm is used for doppler-free spectroscopy of the casesium D$_2$ line. The laser is current-modulated by a Red Pitaya which runs the open-source PDH-locking tool "linien" (https://github.com/hermitdemschoenenleben/linien) and locked to one of

the spectroscopy lines.

A second Red Pitaya is used to stabilize the length of the Fabry-Pérot cavity. Since the demodulation its clock is synchronized with two Red Pitayas by performing an external ADC clock modification detailed in the manufacturer's documentation. This way one modulated laser can be used to generate two error signals by connecting the two devices with a clock synchronization cable.

The input of the second Red Pitaya is connected to the reflection photodiode of the high finesse cavity. Again using the PDH-locking function of "linien" the cavity length is stabilized, as the second Red Pitaya compensates for length variation of the cavity by applying a voltage the piezo stack moving one mirror inside the cavity. Because the output voltage range of $V_{pp} = 2\,\text{V}$ limits the compensation range for longer locking times, a rack-mounted operational amplifier (see chapter 5.3) channel is used for boosting the output voltage.

A third red pitaya is then used to stabilize the main cooling laser. It also uses the reflection photodiode's output from the cavity which is split between the first and the second red pitaya. In the linien locking suite, the modulation frequency is set to a different frequency than the one used for the main cooling laser. This way the one photodiode can be used for two lasers since the demodulation stage will suppress the signal of the other laser with a different modulation frequency. A PDH-lock is used to control the grating voltage of the main cooling laser which is once again amplified by a rack-mounted amplifier.

Linien uses a PID loop to lock the lasers, which is detailed in chapter 2.5.2. By tuning the parameters of the control loop the reponse of the system to acoustic disturbances or vibrations can be vastly improved. For the main cooling laser, these parameters can be optimized by observing the transmission photodiode's output with an oscilloscope. If the laser is properly locked the signal will be increased in comparison to the free-running state. The stability can be tested by manually induced oscillations of the optical table.

4 Summary and Outlook

First, the necessity for a third repump laser in the existing laser cooling setup for BaF has been theoretically motivated. The effects on the modehop-free tuning range in dependency on the placement of the grating have been simulated. To obtain a larger tuning range, a design with two piezos could be implemented future designs [55]. Two piezos can be controlled in such a way, that the conditions in chapter 2.3.3 are satisfied.

Output power and beam profile of the newly constructed repump laser have been characterized. The stability of the wavelength with supply current or temperature variations was measured next. Long-term frequency stability can be achieved with a locking scheme based on the Pound-Drever-Hall method, which was introduced and realized with a FPGA board running the open-source "linien" program.

In order to get a working locking setup, the reflection signal of an optical cavity is needed. As previously remarked by the group, the currently used transfer cavity built by [39] had a broad noise spectrum around the dip in the reflection signal. This noise has destabilized other lasers in the transfer lock in previous locking attempts. Therefore a new small transfer cavity was built after design of [40] and the noise-spectrum was compared. The newly constructed cavity showed vastly better signal to noise ratio and was therefore used for further locking attempts. To further characterize the cavity for potential use in the experiment, the non-linearity of its piezo was measured and a correction polynomial was found.

The long-term stability of the cavity was assessed by a one hour recording of the frequency drift of the cavity measured against a laser which was locked to a spectroscopy line. The drift of 220 MHz has to be compensated for, since such a large drift would mean that the laser's frequencies do no longer overlap with the targeted transitions. This could be achieved by thermally insulating the cavity, by placing it inside a vacuum chamber with optical access through viewports on both sides. Another option would be an active temperature stabilization with a Peltier element.

One disadvantage of the new cavity is the increased $\Delta f_{\mathrm{fsr,tomsch}} = 928.2\,\mathrm{MHz}$ compared to $\Delta f_{\mathrm{fsr,large}} = 75\,\mathrm{MHz}$, which means it can be only locked in frequency steps in these step-widths if the PDH locking scheme is used.

The code which automatically calculates this polynomial can be a platform for future development to perform digital locking of multiple lasers on one cavity, without sideband modulation.

5 Appendix

5.1 Specifications of the laser diode

Taken from the datasheet of the LD-0910-0050-AR-1 diode from Toptica photonics, the linewidth Δv is calculated for the use inside an external cavity diode laser:

$\lambda_{\min}$	$\lambda_{\max}$	$\Delta f_{\mathrm{modehopfree}}$	P	linewidth Δv	Notes
$894\,\mathrm{nm}$	$920\,\mathrm{nm}$	$20\,\mathrm{GHz}$	$40\,\mathrm{mW}$	$100\,\mathrm{kHz}$	$P = 35\,\mathrm{mW},\ \lambda \notin [905\,\mathrm{nm}, 915\,\mathrm{nm}]$

5.2 Protection circuit

The schematic of the assembled laser system can be found in figure 37. The protection circuit next to the diode features a Zener diode 1N5711 which should protect against excessive voltages in the reverse direction of the laser diode. The four 1N4148 diodes have combined forward voltage which is slightly higher than the diode and should protect against electrostatic discharges. Both the 1N5711 and the 1N4148 diode have a diode-capacitance of less than $2\,\mathrm{pF}$ and $4\,\mathrm{pF}$ respectively, making them suitable to protect against ESD.

To modulate the current, a bias tee PBTC-1GW+ from Minicircuits, which combines the DC and modulation input while insulating both inputs against each other, is used.

The Peltier module is controlled by the TED200C temperature controller which regulates the supplied current based on the temperature of the laser assembly, measured by a $10\,\mathrm{k\Omega}$-NTC.
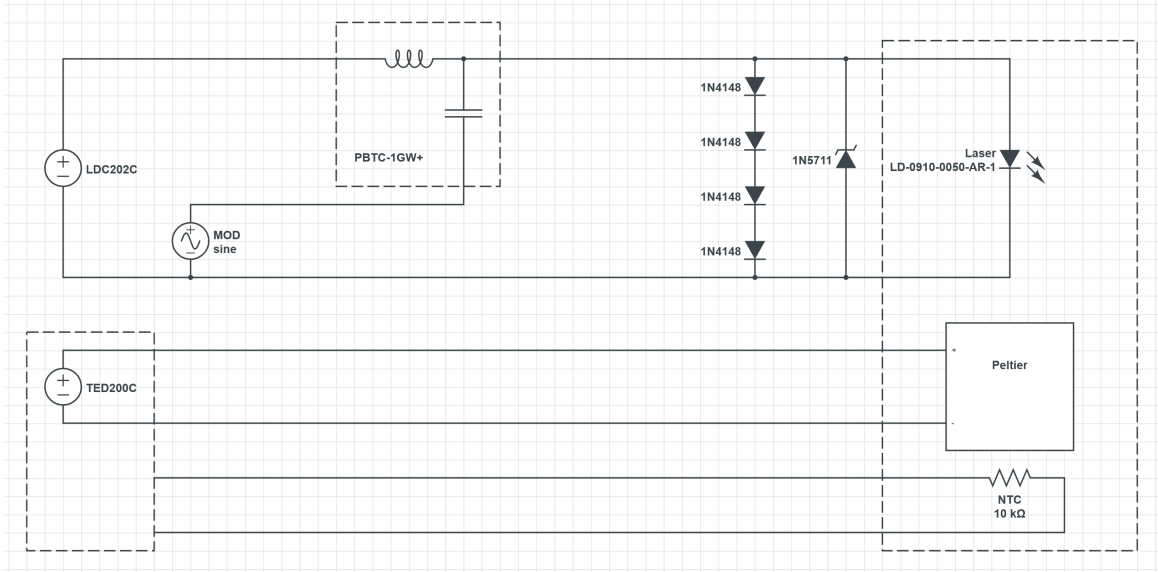
Figure 37: Schematic of the electronics inside the laser

5.3 Amplifiers for the output channels of the Red Pitaya
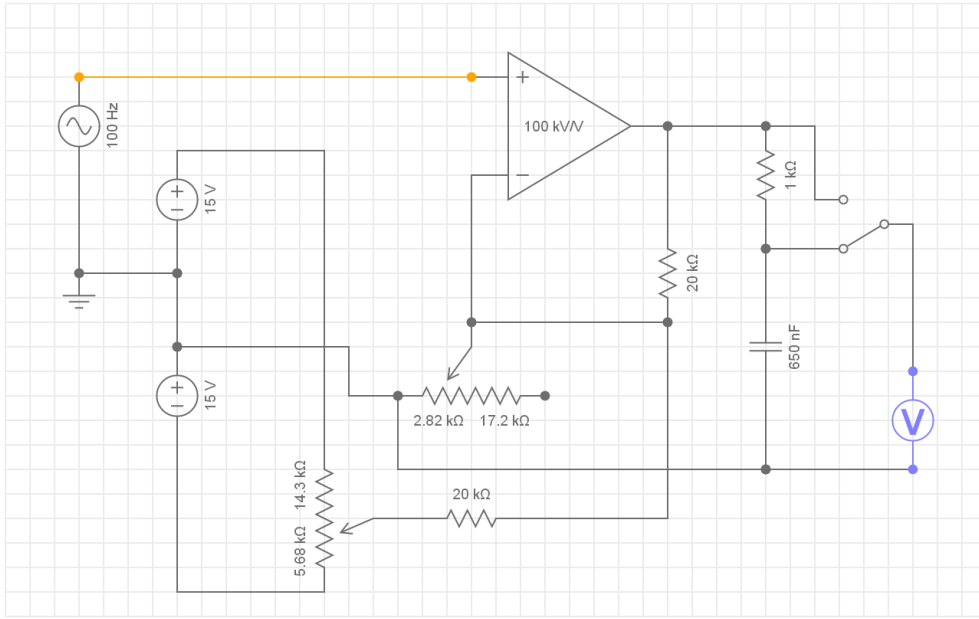
Figure 38: Schematic of a single noninverting amplifier used inside a rack module that has four identical versions of this circuit. The potentiometers control the offset and amplification of the incoming signal. With a jumper on the board, the low pass filter can be removed from the output chain, represented by a switch in the schematic. Because of the non-inverting design, the circuit can produce only gains over 2×.
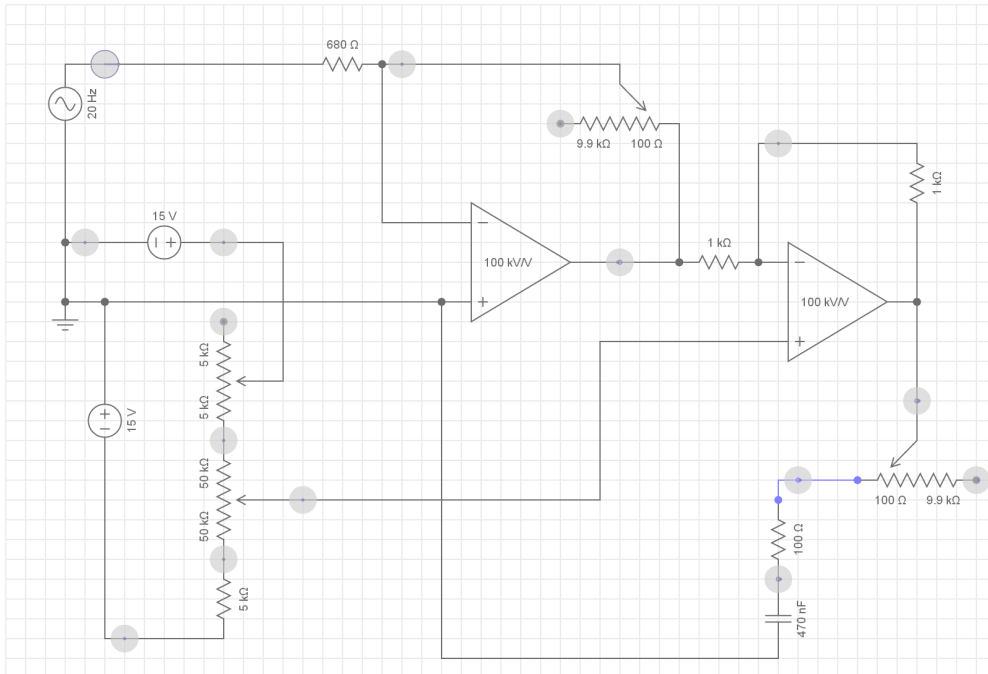

Figure 39: Schematic of a double inverting amplifier circuit which is used, along with an identical copy inside a rack module. In comparison to the amplifier presented in figure 38 this version has a coarse and fine voltage offset adjust potentiometer, as well as a low pass filter which's cutoff-frequency is adjustable.

5.4 Attached code written as part of this thesis

This obviously only works in the digital version, but you will have to run the code on a computer anyways.

5.4.1 Pivot point calculator

This tool does calculate the angles in which the grating of a laser in the PI5 design must be placed on the baseplate. Additionally it generates a map of tuning ranges to asses the position of the grating holder on the baseplate.
click here to extract the python code for pivotcalc.py as text file

5.4.2 Prism simulation

Two prisms with adjustable wedge angle are simulated, so that the input and output ray are parallel.
click here to extract the python code for prismCalc.py as text file

5.4.3 PDH simulation

The reflection signal of a Fabry-Pérot cavity and the phase between the electric field of the first and consecutive reflections is plotted. The PDH signal is generated with adjustable modulation frequency.
click here to extract the python code for pdh.py as text file

5.4.4 DigitalLaserLock / piezo characterisation

Further details provided on the project's github page:
https://github.com/BenjaminRenz/digitalLaserLockPitaya

References

[1] W. Neuhauser et al. "Optical-Sideband Cooling of Visible Atom Cloud Confined in Parabolic Well". In: *Physical Review Letters* 41.4 (July 1978), pp. 233–236. DOI: 10.1103/physrevlett.41.233. URL: https://doi.org/10.1103%2Fphysrevlett.41.233.

[2] "Laser Cooling and Trapping of Atoms". In: *Journal of the Optical Society of America B* 6.11 (Nov. 1989), p. 2020. DOI: 10.1364/josab.6.002020. URL: https://doi.org/10.1364%2Fjosab.6.002020.

[3] E. S. Shuman, J. F. Barry, and D. DeMille. "Laser cooling of a diatomic molecule". In: *Nature* 467.7317 (Sept. 2010), pp. 820–823. DOI: 10.1038/nature09443. URL: https://doi.org/10.1038%2Fnature09443.

[4] S. L. Campbell et al. "A Fermi-degenerate three-dimensional optical lattice clock". In: *Science* 358.6359 (Oct. 2017), pp. 90–94. DOI: 10.1126/science.aam5538. URL: https://doi.org/10.1126%2Fscience.aam5538.

[5] Daniel Barredo et al. "Synthetic three-dimensional atomic structures assembled atom by atom". In: *Nature* 561.7721 (Sept. 2018), pp. 79–82. DOI: 10.1038/s41586-018-0450-2. URL: https://doi.org/10.1038%2Fs41586-018-0450-2.

[6] M. H. Anderson et al. "Observation of Bose-Einstein Condensation in a Dilute Atomic Vapor". In: *Science* 269.5221 (July 1995), pp. 198–201. DOI: 10.1126/science.269.5221.198. URL: https://doi.org/10.1126%2Fscience.269.5221.198.

[7] Immanuel Bloch, Jean Dalibard, and Wilhelm Zwerger. "Many-body physics with ultracold gases". In: *Reviews of Modern Physics* 80.3 (July 2008), pp. 885–964. DOI: 10.1103/revmodphys.80.885. URL: https://doi.org/10.1103%2Frevmodphys.80.885.

[8] Immanuel Bloch, Jean Dalibard, and Sylvain Nascimbène. "Quantum simulations with ultracold quantum gases". In: *Nature Physics* 8.4 (Apr. 2012), pp. 267–276. DOI: 10.1038/nphys2259. URL: https://doi.org/10.1038%2Fnphys2259.

[9] R. V. Krems. "Cold controlled chemistry". In: *Physical Chemistry Chemical Physics* 10.28 (2008), p. 4081. DOI: 10.1039/b802322k. URL: https://doi.org/10.1039%2Fb802322k.

[10] M. S. Safronova et al. "Search for new physics with atoms and molecules". In: *Reviews of Modern Physics* 90.2 (June 2018). DOI: 10.1103/revmodphys.90.025008. URL: https://doi.org/10.1103%2Frevmodphys.90.025008.

[11] "Improved limit on the electric dipole moment of the electron". In: *Nature* 562.7727 (Oct. 2018), pp. 355–360. DOI: 10.1038/s41586-018-0599-8. URL: https://doi.org/10.1038%2Fs41586-018-0599-8.

[12] "Improved limit on the electric dipole moment of the electron". In: *Nature* 562.7727 (Oct. 2018), pp. 355–360. DOI: 10.1038/s41586-018-0599-8. URL: https://doi.org/10.1038%2Fs41586-018-0599-8.

[13] Emine Altuntaş et al. "Demonstration of a Sensitive Method to Measure Nuclear-Spin-Dependent Parity Violation". In: *Physical Review Letters* 120.14 (Apr. 2018). DOI: 10.1103/physrevlett.120.142501. URL: https://doi.org/10.1103%2Fphysrevlett.120.142501.

[14] Lincoln D Carr et al. "Cold and ultracold molecules: science, technology and applications". In: *New Journal of Physics* 11.5 (May 2009), p. 055049. DOI: 10.1088/1367-2630/11/5/055049. URL: https://doi.org/10.1088%2F1367-2630%2F11%2F5%2F055049.

[15] Shuying Kang et al. "The suitability of barium monofluoride for laser cooling from ab initio study". In: *Molecular Physics* 114.6 (Dec. 2015), pp. 810–818. DOI: `10.1080/00268976.2015.1121294`. URL: `https://doi.org/10.1080%2F00268976.2015.1121294`.

[16] Christopher J Foot. *Atomic physics*. Oxford master series in atomic, optical and laser physics. Oxford: Oxford University Press, 2007, p. 180.

[17] Daniel Halwidl. *Development of an Effusive Molecular Beam Apparatus*. Springer Fachmedien Wiesbaden, 2016. DOI: `10.1007/978-3-658-13536-2`. URL: `https://doi.org/10.1007%2F978-3-658-13536-2`.

[18] *Molekülphysik und Quantenchemie*. Springer-Verlag, 2006, p. 273. DOI: `10.1007/3-540-30315-4`. URL: `https://doi.org/10.1007%2F3-540-30315-4`.

[19] Liang Xu et al. "BaF radical: A promising candidate for laser cooling and magneto-optical trapping". In: *Chinese Physics B* 26.3 (Mar. 2017), p. 033702. DOI: `10.1088/1674-1056/26/3/033702`. URL: `https://doi.org/10.1088%2F1674-1056%2F26%2F3%2F033702`.

[20] Ralf Albrecht et al. "Buffer-gas cooling, high-resolution spectroscopy, and optical cycling of barium monofluoride molecules". In: *Physical Review A* 101.1 (Jan. 2020). DOI: `10.1103/physreva.101.013413`. URL: `https://doi.org/10.1103%2Fphysreva.101.013413`.

[21] Tao Chen, Wenhao Bu, and Bo Yan. "Radiative deflection of a BaF molecular beam via optical cycling". In: *Physical Review A* 96.5 (Nov. 2017). DOI: `10.1103/physreva.96.053401`. URL: `https://doi.org/10.1103%2Fphysreva.96.053401`.

[22] *NIST Standard Reference Database 69: NIST Chemistry WebBook*. URL: `https://webbook.nist.gov/cgi/inchi?ID=C13966706`.

[23] K. J. R. Rosman and P. D. P. Taylor. "Isotopic compositions of the elements 1997 (Technical Report)". In: *Pure and Applied Chemistry* 70.1 (Jan. 1998), pp. 221–226. DOI: `10.1351/pac199870010217`. URL: `https://doi.org/10.1351%2Fpac199870010217`.

[24] W. E. Ernst, J. Kändler, and T. Törring. "Hyperfine structure and electric dipole moment of BaF". In: *The Journal of Chemical Physics* 84.9 (May 1986), p. 4772. DOI: `10.1063/1.449961`. URL: `https://doi.org/10.1063%2F1.449961`.

[25] *Tapered Amplifiers for External Cavity Laser Setups*. URL: `http://dilas.com/assets/media/downloads/COHERENT-DILAS_Semi_Tapered_Amplifiers_20180110.pdf`.

[26] Mohammad Memarian, Xiaoqiang Li, and Tatsuo Itoh. "Resonant blazed metasurface gratings". In: *2016 46th European Microwave Conference (EuMC)*. IEEE, Oct. 2016. DOI: `10.1109/eumc.2016.7824337`. URL: `https://doi.org/10.1109%2Feumc.2016.7824337`.

[27] Patrick McNicholl and Harold J. Metcalf. "Synchronous cavity mode and feedback wavelength scanning in dye laser oscillators with gratings". In: *Applied Optics* 24.17 (Sept. 1985), p. 2757. DOI: `10.1364/ao.24.002757`. URL: `https://doi.org/10.1364%2Fao.24.002757`.

[28] Kevin S. Repasky et al. "Extending the continuous tuning range of an external-cavity diode laser". In: *Applied Optics* 45.35 (Dec. 2006), p. 9013. DOI: `10.1364/ao.45.009013`. URL: `https://doi.org/10.1364%2Fao.45.009013`.

[29] Xiaodong Wang, Bryan Fox, and Ronald J. Vernon. "Spatial modifications of a Gaussian beam incident on a diffraction grating". In: *Journal of the Optical Society of America A* 36.4 (Mar. 2019), p. 498. DOI: `10.1364/josaa.36.000498`. URL: `https://doi.org/10.1364%2Fjosaa.36.000498`.

[30] RAYLEIGH. "On the Magnetic Rotation of Light and the Second Law of Thermo-Dynamics". In: *Nature* 64.1667 (Oct. 1901), pp. 577–578. DOI: 10.1038/064577e0. URL: https://doi.org/10.1038%2F064577e0.

[31] Hanne Ludvigsen, Mika Tossavainen, and Matti Kaivola. "Laser linewidth measurements using self-homodyne detection with short delay". In: *Optics Communications* 155.1-3 (Oct. 1998), pp. 180–186. DOI: 10.1016/s0030-4018(98)00355-1. URL: https://doi.org/10.1016%2Fs0030-4018%2898%2900355-1.

[32] Dr. Rüdiger Paschotta. *Coherence Time.* URL: https://www.rp-photonics.com/coherence_time.html.

[33] K. Razdan and D. A. Van Baak. "Demonstrating optical beat notes through heterodyne experiments". In: *American Journal of Physics* 70.10 (Oct. 2002), pp. 1061–1067. DOI: 10.1119/1.1484150. URL: https://doi.org/10.1119%2F1.1484150.

[34] J.J. Olivero and R.L. Longbothum. "Empirical fits to the Voigt line width: A brief review". In: *Journal of Quantitative Spectroscopy and Radiative Transfer* 17.2 (Feb. 1977), pp. 233–236. DOI: 10.1016/0022-4073(77)90161-3. URL: https://doi.org/10.1016%2F0022-4073%2877%2990161-3.

[35] V. B. Tiwari et al. "Laser frequency stabilization and large detuning by Doppler-free dichroic lock technique: Application to atom cooling". In: *Pramana* 65.3 (Sept. 2005), pp. 403–411. DOI: 10.1007/bf02704199. URL: https://doi.org/10.1007%2Fbf02704199.

[36] G. D. Boyd and H. Kogelnik. "Generalized Confocal Resonator Theory". In: *Bell System Technical Journal* 41.4 (July 1962), p. 1364. DOI: 10.1002/j.1538-7305.1962.tb03281.x. URL: https://doi.org/10.1002%2Fj.1538-7305.1962.tb03281.x.

[37] Nur Ismail et al. "Fabry-Pérot resonator: spectral line shapes, generic and related Airy distributions, linewidths, finesses, and performance at low or frequency-dependent reflectivity". In: *Optics Express* 24.15 (July 2016), p. 16366. DOI: 10.1364/oe.24.016366. URL: https://doi.org/10.1364%2Foe.24.016366.

[38] *Fabry-Perot Tutorial.* URL: https://www.thorlabs.com/tutorials.cfm?tabID=E9D2D96F-1EFD-4EF0-BB17-FA2CA60F8A8D.

[39] Maximilian Meister. "Setup of a stable reference cavity for laser spectroscopy". diploma thesis. 5th institute of physics - university of stuttgart, July 2, 2008.

[40] Christian Tomschitz. "A photoionization scheme to create coldionic impurities from Rydberg atoms". master thesis. 5th institute of physics - university of stuttgart, Oct. 23, 2018. URL: https://www.pi5.uni-stuttgart.de/documents/abgeschlossene-arbeiten/2018-Tomschitz-Christian-A-photoionization-scheme-to-create-cold-ionic-impurities-from-Rydberg-atoms-MSC.pdf.

[41] Kiam Heong Ang, G. Chong, and Yun Li. "PID control system analysis, design, and technology". In: *IEEE Transactions on Control Systems Technology* 13.4 (July 2005), pp. 559–576. DOI: 10.1109/tcst.2005.847331. URL: https://doi.org/10.1109%2Ftcst.2005.847331.

[42] A.J. Isaksson and S.F. Graebe. "Derivative filter is an integral part of PID design". In: *IEE Proceedings - Control Theory and Applications* 149.1 (Jan. 2002), pp. 41–45. DOI: 10.1049/ip-cta:20020111. URL: https://doi.org/10.1049%2Fip-cta%3A20020111.

[43] Tore Hägglund. "A unified discussion on signal filtering in PID control". In: *Control Engineering Practice* 21.8 (Aug. 2013), pp. 994–1006. DOI: 10.1016/j.conengprac.2013.03.012. URL: https://doi.org/10.1016%2Fj.conengprac.2013.03.012.

[44] R. W. P. Drever et al. "Laser phase and frequency stabilization using an optical resonator". In: *Applied Physics B Photophysics and Laser Chemistry* 31.2 (June 1983), pp. 97–105. DOI: 10.1007/bf00702605. URL: https://doi.org/10.1007%2Fbf00702605.

[45] Eric D. Black. "An introduction to Pound–Drever–Hall laser frequency stabilization". In: *American Journal of Physics* 69.1 (Jan. 2001), p. 80. DOI: 10.1119/1.1286663. URL: https://doi.org/10.1119%2F1.1286663.

[46] Max Born et al. *Principles of Optics*. Cambridge University Press, Oct. 1999, p. 325. DOI: 10.1017/cbo9781139644181. URL: https://doi.org/10.1017%2Fcbo9781139644181.

[47] Luis L Sánchez-Soto, Juan J Monzón, and Gerd Leuchs. "The many facets of the Fabry–Perot". In: *European Journal of Physics* 37.6 (Sept. 2016), p. 064001. DOI: 10.1088/0143-0807/37/6/064001. URL: https://doi.org/10.1088%2F0143-0807%2F37%2F6%2F064001.

[48] Christian Tomschitz. "Aufbau eines Diodenlasers zur hochaufloesenden Spektroskopie von Lithium". bachelor thesis. Aug. 5, 2016. URL: https://www.pi5.uni-stuttgart.de/documents/abgeschlossene-arbeiten/2016-Tomschitz-Christian-Aufbau-eines-Diodenlasers-zur-hochaufloesenden-Spektroskopie-von-Lithium-BSC.pdf.

[49] Haiyin Sun. *A Practical Guide to Handling Laser Diode Beams*. Springer Netherlands, 2015. DOI: 10.1007/978-94-017-9783-2. URL: https://doi.org/10.1007%2F978-94-017-9783-2.

[50] *Beam Circularization Lab Fact*. URL: https://www.thorlabs.com/newgrouppage9.cfm?objectgroup_id=11426.

[51] *Laser Beam Profiles*. URL: https://www.laserglow.com/content/Laser-Beam-Profiles.

[52] Yu Peng. "A Novel Scheme for Hundred-Hertz Linewidth Measurements with the Self-Heterodyne Method". In: *Chinese Physics Letters* 30.8 (Aug. 2013), p. 084208. DOI: 10.1088/0256-307x/30/8/084208. URL: https://doi.org/10.1088%2F0256-307x%2F30%2F8%2F084208.

[53] Dr. Rüdiger Paschotta. *External-cavity diode lasers*. URL: https://www.rp-photonics.com/external_cavity_diode_lasers.html.

[54] Rethwisch David Callister William. *Materials Science and Engineering - An Introduction*. 8th ed. 2009. ISBN: 0-470-41997-0.

[55] Johan Hult, Iain S. Burns, and Clemens F. Kaminski. "Wide-bandwidth mode-hop-free tuning of extended-cavity GaN diode lasers". In: *Applied Optics* 44.18 (June 2005), p. 3675. DOI: 10.1364/ao.44.003675. URL: https://doi.org/10.1364%2Fao.44.003675.

Acknowledgments

The thesis has been made possible with support from the following people. I would like to thank